ABSTRACT

Title of Thesis: EXPERIMENTAL INVESTIGATION OF BOUNDARY LAYER TRANSITION ON CONE-FLARE GEOMETRIES AT MACH 4

Gavin W. Norris
Master of Science, 2024

Thesis Directed By: Dr. Stuart Laurence, Associate Professor
Department of Aerospace Engineering

This study investigates supersonic boundary layer transition on a cone-flare with a 5° half-angle straight cone and flared bases of +5°, +10°, and +15°. The experiments used the University of Maryland's Multiphase Flow Investigations Tunnel (MIST), a Mach 4 Ludweig tube. Experiments were performed “dry”, without aerosols or droplets, and focus on the first-mode (Tollmien-Schlichting) boundary layer instability waves and their interaction with the compression corner. Using high-speed Schlieren imaging, the boundary layer dynamics on the cone-flare's top surface were analyzed. The data were processed through Power Spectral Density (PSD) and Spectral Proper Orthogonal Decomposition (SPOD) techniques to study the behavior of the first-mode waves and the transition location changes. The findings reveal coherent wave packets within the boundary layer at frequencies characteristic of the first-mode. The wave packets power increased along the cone

and peaked near the compression corner before dissipation on the flare. These findings contribute to the understanding of first-mode boundary layer transition mechanisms in hypersonic flows for the cone-flare geometry.

EXPERIMENTAL INVESTIGATION OF BOUNDARY LAYER TRANSITION ON CONE-FLARE GEOMETRIES AT MACH 4

by

Gavin W. Norris

Thesis submitted to the Faculty of the Graduate School of the
University of Maryland, College Park, in partial fulfillment
of the requirements for the degree of
Master of Science
2024

Advisory Committee:
Professor Stuart Laurence, Chair
Professor Kenneth Yu
Professor Christopher Cadou

Acknowledgements

I am profoundly grateful for the support and inspiration I have received throughout my career and during my time at the University of Maryland. I am deeply grateful for the unwavering love and support of my beautiful wife, whose encouragement made this experience possible. I am also thankful for the support of my parents, siblings, and extended family, especially my grandfather, whose passion for engineering ignited my own interest in the field.

I extend my sincere gratitude to Dr. Stuart Laurence for his expert guidance throughout my graduate studies. I am also indebted to Antonio Schöneich for his invaluable assistance in operating the MIST facility, to Dr. Hassan Ifti for his mentorship and for sharing his vast research experience, and to Dr. Cole Sousa, whose data analysis expertise was crucial to the findings presented in this study. Each of these individuals has made a lasting impact on my education and career, and I am deeply thankful for their contributions.

Table of Contents

List of Tables

List of Figures

Chapter 1: Introduction

1.1 Motivation

The United States is intensifying its efforts in hypersonic missile development due to advancements by key rivals. Russia notably operationally deployed the first hypersonic missile during its recent military action in Ukraine [1]. Consequently, the Department of Defense has been funding research and development for two types of hypersonic missiles: boost-glide and air-breathing cruise vehicles [2, 3]. Both types of missiles operate within the stratosphere at sustained hypersonic speeds. This continuous hypersonic flight subjects the vehicle to severe aerothermal stress, making thermal management one of the driving aspects of vehicle design.

Despite extensive research on hypersonic boundary layer transition, significant uncertainties persist, especially for complex geometries [4]. The transition of the boundary layer from laminar to turbulent can dramatically increase viscous heating rates by up to eight times [5, 6]. Understanding where, how and why the boundary layer transitions to turbulence will aid in hypersonic vehicle design. Incomplete understanding of boundary layer transitions results in oversized thermal protection systems which increase vehicle mass and volume.

This research investigates boundary layer transition on a 5° half-angle cone with flared bases of +5°, +10°, and +15° at Mach 4, utilizing Schlieren imaging and advanced data analysis techniques. The sudden change in surface angle in these geometries is representative of engine intakes, control surfaces and various other vehicle geometries. By studying the boundary layer under these conditions and

employing visualization and spectral analysis methods, this work aims to identify and characterize the dominant instability modes and the impact of the flared base geometry. This study enhances the understanding of boundary layer transition behavior over the cone-flare geometry, which is essential for hypersonic vehicle design.

1.2 Historical Boundary Layer Studies

The foundational theories of laminar flow instabilities began with Lord Rayleigh in the late 1800s, highlighting the instability of certain inviscid flows to small disturbances [7]. Extending these concepts, Ludwig Prandtl and his students developed a viscous theory that predicted the growth of vortical waves in shear flows [8]. This theory was initially dismissed until the experimental discovery of Tollmien-Schlichting waves by Schubauer and Skramstad in 1947 [9-11]. This discovery revitalized the field, spurring extensive research that has since employed theoretical, experimental, and computational approaches.

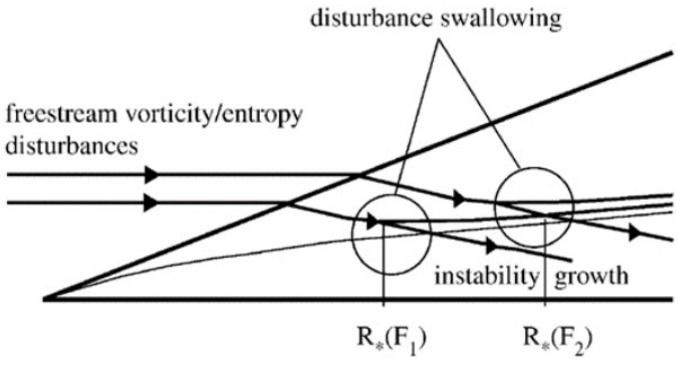

Figure 1.1: Graphic of boundary layer receptive region [24]

Boundary layer transition can be induced by various mechanisms, including freestream disturbances such as vorticity, acoustic, and entropy waves [24-26]. Figure

1.2 below illustrates the various paths these disturbances can take to causing breakdown of the boundary layer to turbulence [24].

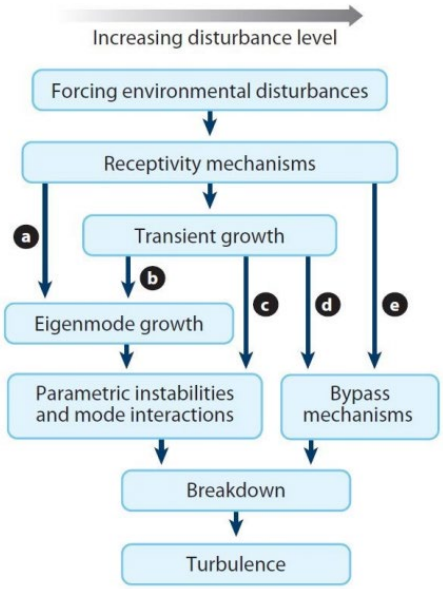

Figure 1.2: Paths to turbulence in boundary layer flows [26]

In the realm of high-speed aerodynamics, particularly at Mach 4, understanding the behavior of two key instability modes within the boundary layer is crucial. These modes are the first-mode Tollmien-Schlichting (TS) waves and the second "Mack" mode disturbances, both of which are critical for understanding transition processes. The TS waves, first identified in theoretical work by Taylor, Tollmien, and Schlichting, are first-mode instability waves that typically manifest at frequencies ranging from tens to a few hundreds of kHz [12]. These first-mode waves primarily result from the interaction of viscous forces within the boundary layer and are the compressible analog of the incompressible TS waves [13-16].

In contrast, the second-mode, known as Mack mode disturbances, appear at higher frequencies, from hundreds of kHz to MHz, and their dominance in causing

transition increases with the Mach number [17]. These waves are acoustic in nature [18]. Both instability modes are present at Mach 4, (see figure 1.3) marking it as a critical flow regime for study due to the transition from dominance of one mode to another [17-19].

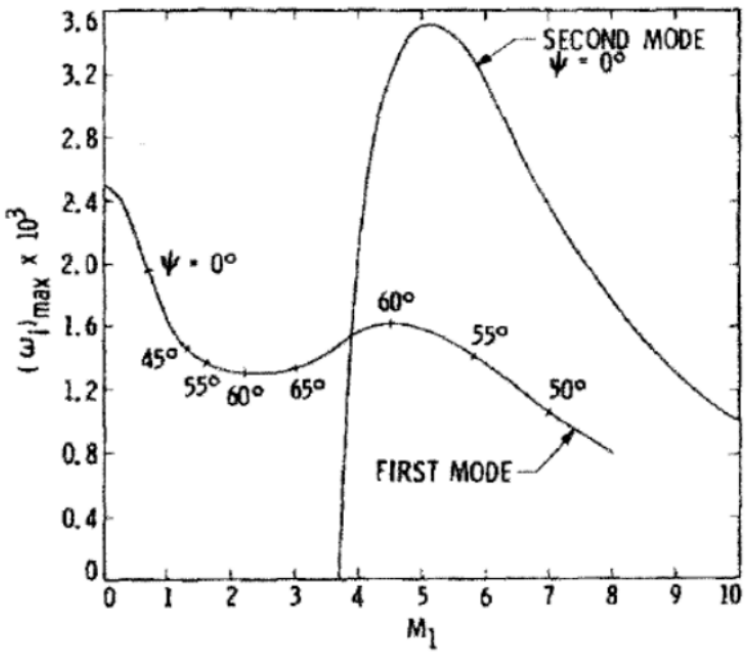

Figure 1.3: Mack instability modes spatial amplification rate as a function of freestream Mach number at Re = 1500 [19]

This study examines how variations in the geometry of a cone's flared base influence how first-mode waves propagate along the boundary layer and the impact they have on boundary layer transition. This investigation builds on prior research by Butler, Sousa, and Laurence on cone-flare geometry at higher Mach numbers, which concentrated on Mack mode and higher mode instabilities [20-23]. The study found that a +5° flare angle led to attached flow dominated by second-mode disturbances, encouraging transition of incoming wave packets. For the +15° case, lower-frequency shear-layer disturbances prevailed, especially at lower Reynolds numbers. The +10°

cases exhibited a mix of second-mode and shear-layer disturbances, with significant amplification near reattachment [20]. Finally, at low Reynolds numbers, the boundary layer remained weakly transitional through separation and reattachment. At higher Reynolds numbers, second-mode waves broke down immediately at reattachment, leading to a predominantly turbulent boundary layer [23]. This study focuses on the first-mode instability.

Chapter 2: Methodology

2.1 Facility and Test Conditions

Testing occurred at the University of Maryland's High-Speed Aerodynamics and Propulsion Lab (HAPL), within the Multi-phase Investigations Supersonic Tunnel (MIST) that operates at a Mach 4. Each flare angle was tested at varying Reynolds numbers to gather extensive data for analysis. These experiments were performed without the introduction of droplet flow to isolate and analyze aerodynamic effects inherent to the cone-flare geometries under study.

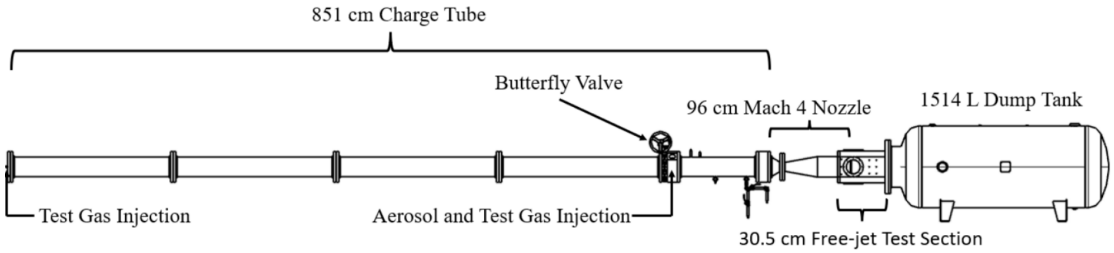

Figure 2.1: MIST side view [26]

To conduct multi-phase flow experiments, the University of Maryland's High-Speed Aerodynamics and Propulsion Lab (HAPL) developed the Multi-phase Investigations Supersonic Tunnel (MIST) in 2023. This specialized Ludweig tube,

designed and constructed by Ph.D. student Antonio Schöneich, uses a fast-acting valve driven by a compressed air piston to initiate flow. MIST features an 851 cm long charge tube with a 20.3 cm diameter, filled with nitrogen, and uses a Mach 4 converging-diverging nozzle with a 6 cm throat and 20.8 cm exit diameter. The nozzle connects to a 30.5 cm diameter free-jet test section, equipped with two 15.2 cm diameter NBK7 windows on each side of the model mount [27]. The setup allows for a nominally steady test duration of approximately 20 ms as seen in Figure 2.2 from time, t = 0.12 s to 0.14 s. This test duration along with other tunnel characteristics was determined with a comprehensive Pitot-Rake study that was conducted across a range of Reynolds numbers. The results from the relevant flow conditions in this study are presented in Figures 2.2 and 2.3 [27]. All experimental runs were conducted at an average ambient temperature of 296 K, resulting in a freestream Mach number of 4.02.

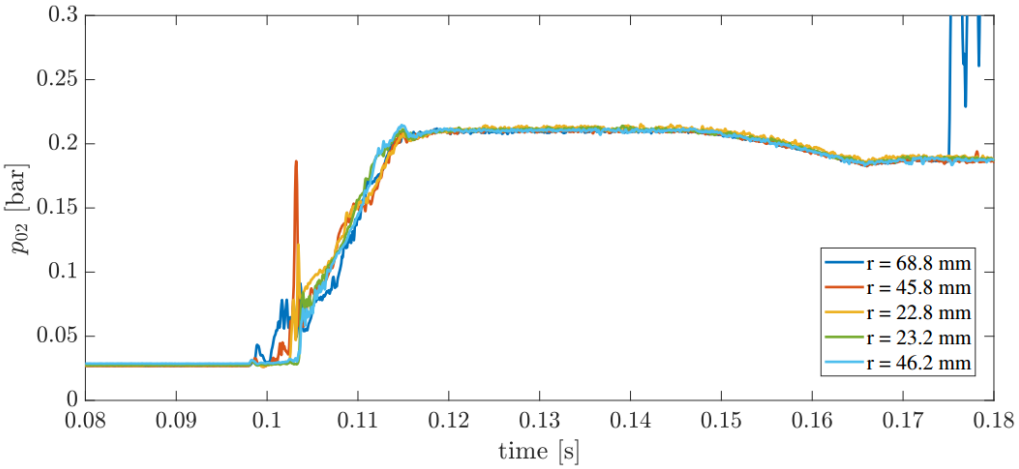

Figure 2.2: MIST Pitot-rake study pressure traces. The region from t = 0.12 to 0.14 seconds indicates an approximately 20 ms steady test time [27].

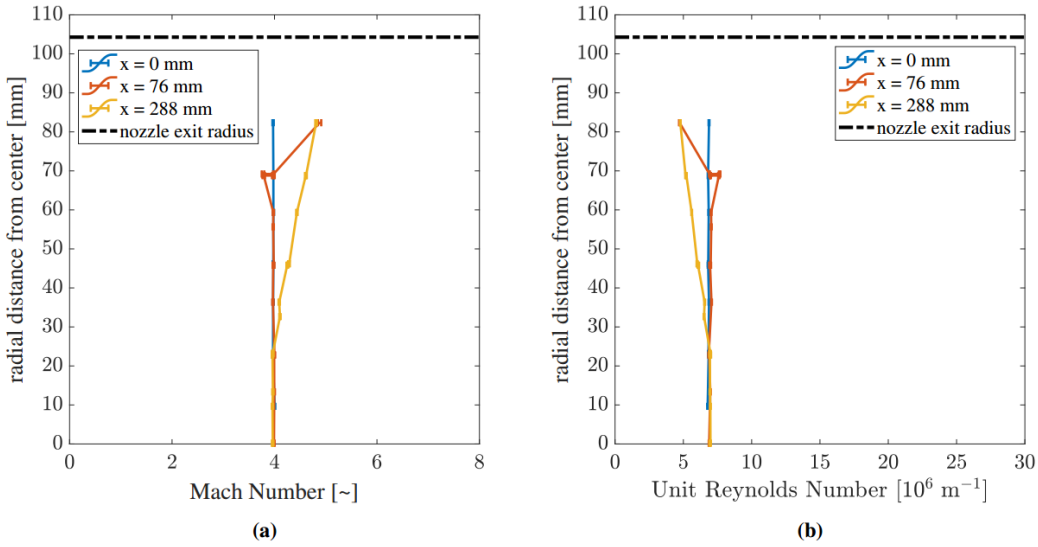

Figure 2.3: (a) Mach number and (b) Reynolds number for a charge tube pressure of 1.5 bar [27]

The experimental study was designed to examine the effects of varying Reynolds numbers (Re) on the boundary layer transition along the flare or cone. For clarity and consistency throughout this paper, Reynolds numbers are presented as Re = X.XX, where X.XX represents the unit Reynolds number multiplied by 10^6 m^{-1}. A range of Reynolds numbers were achieved by adjusting the charge tube pressure, which directly influenced the location of the boundary layer transition. The maximum charge tube pressure utilized was 2.0 bar, corresponding to a unit Reynolds number of Re = 8.95, while the minimum pressure was 1.0 bar, resulting in a Re = 4.47. At an intermediate Reynolds number, Re = 6.27, the flow was completely laminar along the cone surface and transitioned to turbulence along the flare for both the +5° and +10° test cases. At the lowest Reynolds number, Re = 4.47, the +15° flare exhibits similar behavior. Therefore, the results presented show the analyses of all flare angles at Re = 6.27 and a brief discussion of the +15° flare at Re = 4.47.

Table 2.1: Flow conditions for the flow unit Reynolds Numbers examined

Charge Tube Pressure (bar)	**Flow Unit Reynolds Number (10^6 m^{-1})**	p_∞ (10^{-3} bar)	ρ_∞ (10^{-3} $\frac{kg}{m^3}$)	p_0 (bar)	T_∞ (K)	M_∞
1.0	4.48	6.0	29.4	0.93	68.5	4.02
1.4	6.27	8.4	41.1	1.30	68.5	4.02

2.2 Cone-Flare Model

The study was conducted using a 5-degree half-angle cone with flared bases at increments of +5°, +10°, and +15°. The half-angle cone forebody is entirely stainless steel with a nominally sharp nose of 0.10 mm radius [20]. The cone forebody has a length of 150 mm and has a threaded rod to attach the bases. The bases were fabricated from polylactic acid (PLA+) material through fused deposition modeling (FDM), designed for integration with a zero-degree angle of attack tunnel mount. The ridges between layers of the PLA+ inherent in FDM were sanded and polished to a smooth finish to ensure surface roughness would not impact the results. The +10° and +15° bases have a length of 85 mm and the +5° base has a length of 130 mm. The side profile and dimensions of the sharp-nosed cone with +10° base are shown in figure 2.4. The three cone-flare geometries and the zero-degree angle of attack tunnel mount are shown in figure 2.5. This cone-flare geometry is smaller than models used in similar experiments by Butler and Sousa, whose model had a length of 486.2 mm [20]. Due primarily to MIST's smaller nozzle and lower Mach number, earlier tests of the larger

model generated a leading shock that impinged on and reflected off the test section walls, which resulted in highly unsteady flow throughout the test duration.

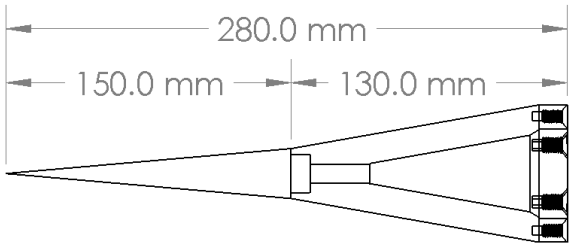

Figure 2.4: Drawing of the +10° Cone-Flare model with dimensions

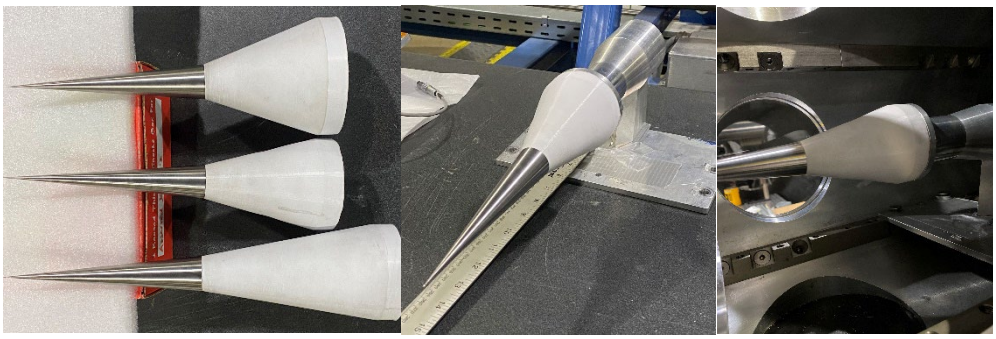

(a) (b) (c)

Figure 2.5: Images of (a) all three flare angles, (b) the +10° flare attached to the mount, and (c) the +10° flare mounted in the test section

The angle of attack was measured to be 0° ± 0.1°, in relation to the freestream, with a digital protractor on the camera and on the test section. The angles of the upper and lower cone surface were measured with image-processing techniques applied to flow-off images to be +5° ± 0.05° and -5° ± 0.05°, respectively.

2.3 Schlieren Visualization

Schlieren imaging was the primary diagnostic used to observe and measure the boundary layer waves on the model. The imaging setup comprised a standard Z-type

configuration with a horizontal knife edge as illustrated in figure 2.6. Spherical mirrors with a focal length of 60 inches and a diameter of 152 mm were used in conjunction with a Cavilux HF laser, which provided illumination with a 20 ns pulse width. Image capture was performed using a Phantom v2512 camera, operating at a frame rate of 270,000 fps. To focus on the steady-state test period, data was truncated to include only frames captured within a 20 ms window. This resulted in approximately 5400 frames per test case. The use of a 12-bit camera reduced the potential for data saturation and increased the dynamic range of the measured pixel intensity signal.

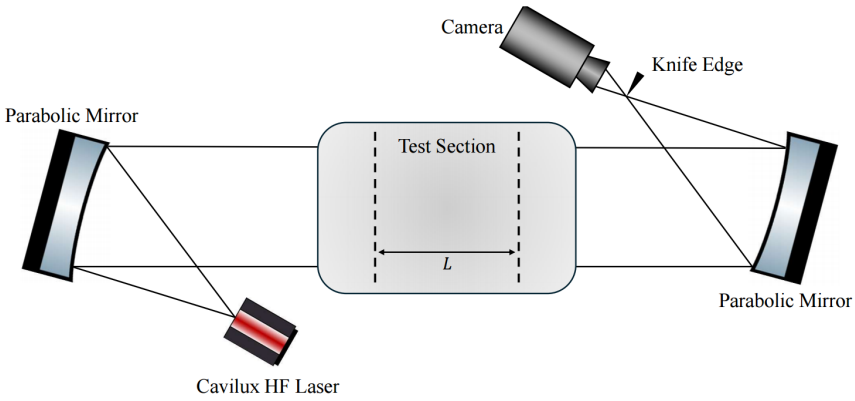

Figure 2.6: Typical Z-type schlieren setup viewed from above

To ensure optical stability, all components of the imaging setup were mounted on optical tables and realigned daily prior to testing. The camera orientation was adjusted to optimize the view of both the cone and the flare within the test section window while maintaining the maximum possible frame rate. A 500 mm plano-convex lens was positioned after the knife edge to increase the resolution of the boundary layer to approximately 10 pixels in height. Since the model, and consequently the area of interest, are relatively small, magnification was needed to ensure enough spatial data

was collected within the boundary layer to identify and characterize the first-mode wave packets. Figure 2.7 shows the placement of the planoconvex lens and location of the camera with respect to the knife edge within the test setup.

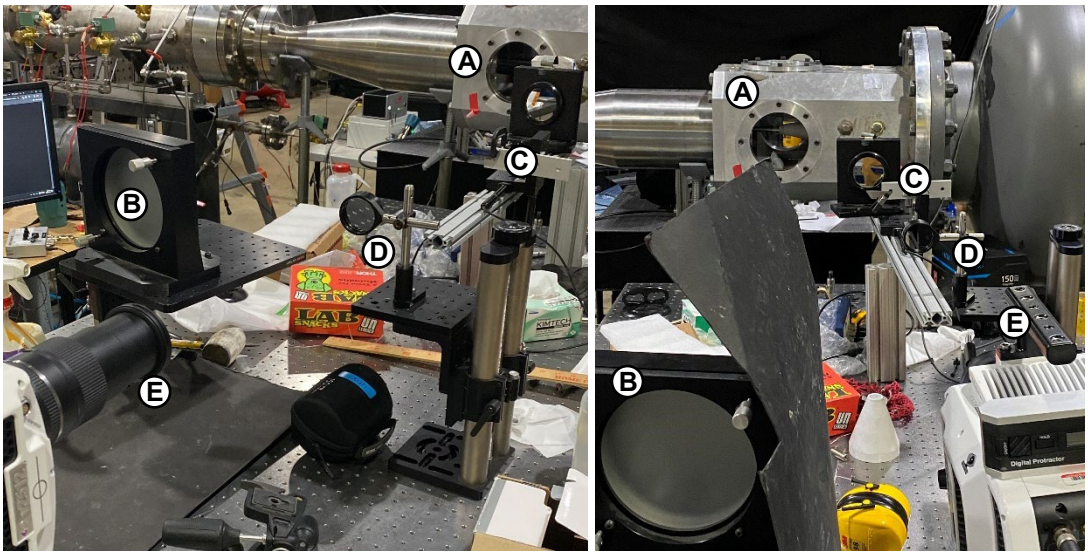

Figure 2.7: Two views of the Schlieren setup showing the (a) test section, (b) spherical lens, (c) knife edge, (d) plano-convex lens and (e) high speed camera

The viewing window for the imaging system was set to 1024 x 80 pixels, with each pixel corresponding to 0.082 mm. This resulted in a field of view of 83.97 mm in the freestream x-direction by 6.56 mm in the y-direction as shown in figure 2.8. With the compression corner placed in the middle of the field of view, the x-direction imaged spans from x = 108 mm to 192 mm from the leading edge, with a small variation depending on flare angle. Calibration of the imaging scale was achieved by placing a screw with a known diameter atop the cone to establish a reference scale factor as shown in figure 2.9.

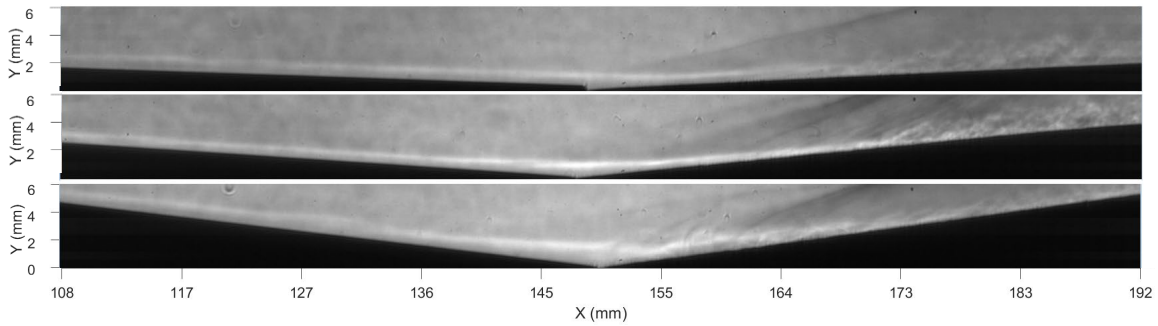

Figure 2.8: Raw schlieren data showing how the camera was angled to maximize capture of the flow, the cone, and the flare. Flow is from left to right.

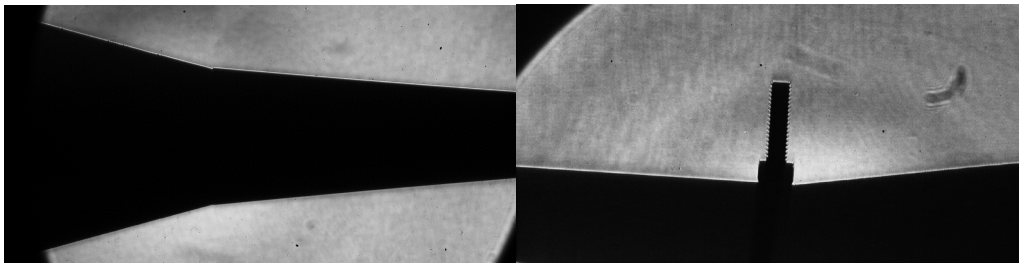

(a) (b)

Figure 2.9: Reference images used to determine (a) angle of attack and (b) pixel size using a screw with a head diameter of 6.72 mm

2.4 Analysis Techniques

Background subtraction was applied to all image data. Each pixel's intensity value was averaged over time and that value was then subtracted from each frame. This highlights moving objects from the static background, which allows for clear visual identification of fluid structures. Figure 2.10 compares a background-subtracted image to raw data, illustrating the technique's ability to differentiate unsteady fluid structures from the static background. This data processing technique improves the clarity of flow features and increases the signal-to-noise ratio for subsequent analysis.

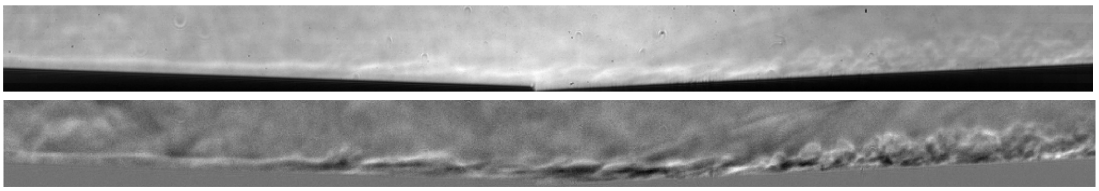

Figure 2.10: Comparison of raw schlieren footage (top) with a background subtracted image (bottom)

2.4.1 Power Spectral Density (PSD)

Power Spectral Density (PSD) analysis is a powerful tool for identifying and quantifying first-mode instability waves within the boundary layer. PSD reveals how the power of a signal is distributed across different frequencies [28, 29]. Mathematically, it is defined as the expected value of the squared magnitude of a signal's Fourier Transform divided by the observation time. However, direct calculation of PSD on noisy data can be unreliable. Welch's method refines this process by segmenting the time-series data from boundary layer measurements into overlapping windows. A window function (e.g., Hamming) is applied to each segment to reduce spectral leakage, followed by a Fourier Transform to obtain a periodogram. Averaging these periodograms enhances signal resolution and reduces noise, significantly improving the detection of high-frequency components. This approach delivers reliable insights into the dynamics and behavior of flow structures within the boundary layer, even in the presence of noise like that found in Schlieren images.

Seven x-locations, consistent across all flare angles, were sampled within the boundary layer. Measured from the cone tip, these locations are at x = 110, 123, 137, 149, 164, 178, and 190 mm. The first three locations lie on the cone body, the fourth directly between the cone and flare, and the final three along the flare itself. For each x-location, y-coordinates were chosen based on the boundary layer thickness. A 3 x 3

grid of pixels was formed around each selected point (y-1:y+1; x-1:x+1). Each pixel within this grid was treated as an independent sensor for analysis using Welch's method. To obtain a representative PSD plot for each boundary layer location, the resulting PSDs of all 9 pixels were averaged. Additionally, a spatial PSD was calculated by applying Welch's method for every pixel in the image. Then the power was summed across a set frequency range and plotted for increased visualization of how the first-mode waves grow within the boundary layer. Each use of Welch's method presented here used 32 frequency bins, a Hamming window for each segment, and 50% overlap between segments.

2.4.2 Spectral Proper Orthogonal Decomposition (SPOD)

Spectral Proper Orthogonal Decomposition (SPOD) is a data-driven modal decomposition technique designed to extract spatiotemporally coherent structures from time-resolved flow field data. This method advances beyond traditional "space-only" Proper Orthogonal Decomposition (POD), which focuses solely on spatial coherence by extracting structures orthogonal under a spatial inner product to optimally represent spatial variance within the flow field. Unlike "space-only" POD, where modes may contain multiple frequency contributions, SPOD conducts decomposition in the frequency domain, isolating sets of modes that oscillate at single frequencies and optimally represent the spatiotemporal statistics of the flow [30].

A state vector, $\mathbf{q(x,t)}$, represents the relevant flow variables at a spatial location $\mathbf{x}$ and time $\mathbf{t}$. A collection of these state vectors over a time interval forms a data matrix,

Q. SPOD begins by segmenting **Q** into overlapping blocks and applying the Discrete Fourier Transform (DFT) to each block:

$$\widehat{q_k}(\omega) = \sum_{t=0}^{N-1} q(t) e^{-2\pi i \omega t/N}$$

where ω is the frequency, N is the block length, and $\widehat{q_k}(\omega)$ represents the Fourier coefficients. Next, the cross-spectral density (CSD) matrix is estimated using Welch's method:

$$\mathrm{S}(\omega) = \frac{1}{\mathrm{K}} \sum_{\mathrm{k}=1}^{\mathrm{K}} \widehat{\mathbf{q}_k}(\omega)\, \widehat{\mathbf{q}_k^*}(\omega)$$

where K is the number of blocks, and the asterisk denotes the complex conjugate transpose. Finally, the SPOD modes, $\mathbf{\Phi(x,\omega)}$, are obtained through eigenvalue decomposition of the CSD matrix at each frequency:

$$S(\omega)\Phi(\omega) = \Phi(\omega)\Lambda(\omega)$$

where $\mathbf{\Lambda(\omega)}$ is a diagonal matrix containing the eigenvalues, which represent the modal energies. SPOD modes are orthogonal and optimally represent the spatiotemporal statistics of the flow at each frequency.

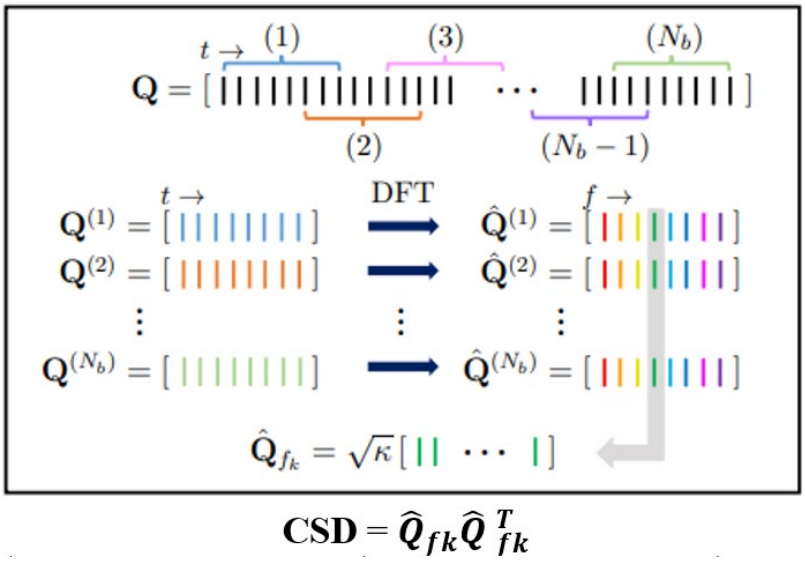

Figure 2.11: Representation of performing SPOD on a dataset [32]

Utilizing SPOD to visualize the fluid structures along each geometry will decompose the flow data into modes that represent their structure and strength at discrete frequencies [32]. This allows for clear visualization of the first-mode waves, revealing their wave patterns, as well as indirectly revealing propagation direction, and growth rate within the boundary layer. It will also reveal how these waves break down after encountering the flare. This technique effectively filters out noise in the data, providing a more focused analysis at specific frequencies of interest. For all SPOD analysis presented a window length of 256 was input to a Hamming window along with 50% overlap between windows.

Chapter 3: Results

3.1 Schlieren Images

Pixel intensity time series from the processed images served as inputs for Power Spectral Density (PSD) and Spectral Proper Orthogonal Decomposition (SPOD) algorithms. These techniques facilitate the extraction of dominant frequencies and coherent flow structures, revealing the spatiotemporal characteristics of the flow dynamics. At these flow conditions the first-mode frequencies tend to be less than 100 kHz. Therefore, the camera frame rate of 270,000 fps is adequate for resolving the relevant frequencies without exceeding the Nyquist limit of 135 kHz. Background subtracted frames from each test case are presented below (figure 3.1-3.3) with 7.4 μs (2 frames) between each image and the cone-flare surface denoted by the dashed green line.

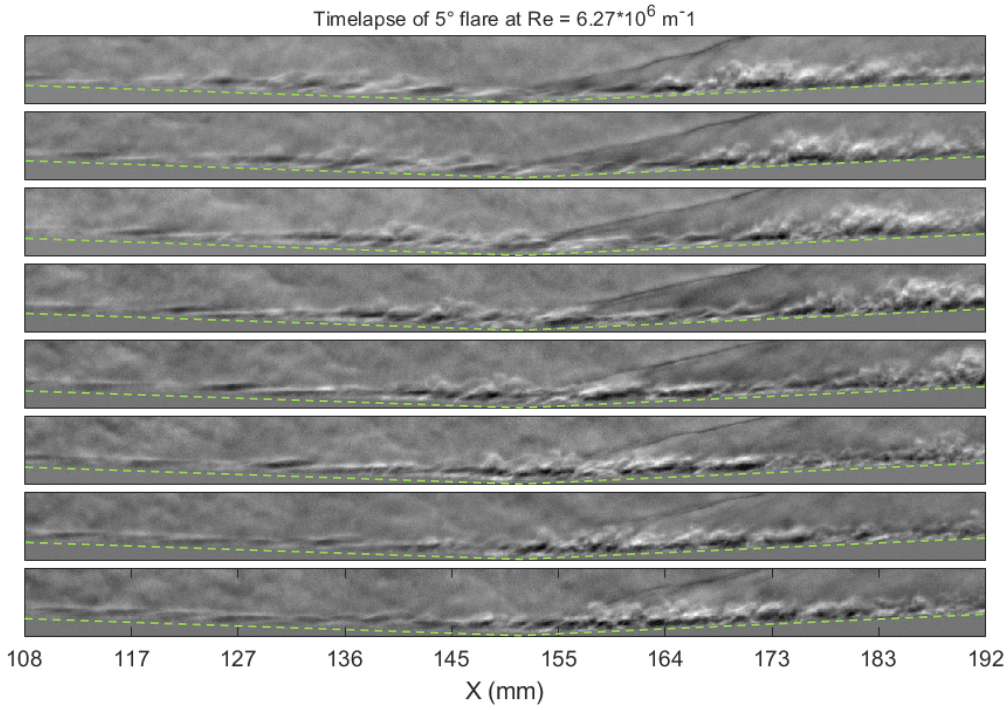

Figure 3.1: Background subtracted timelapse of +5° flare, images are 7.4 μs apart

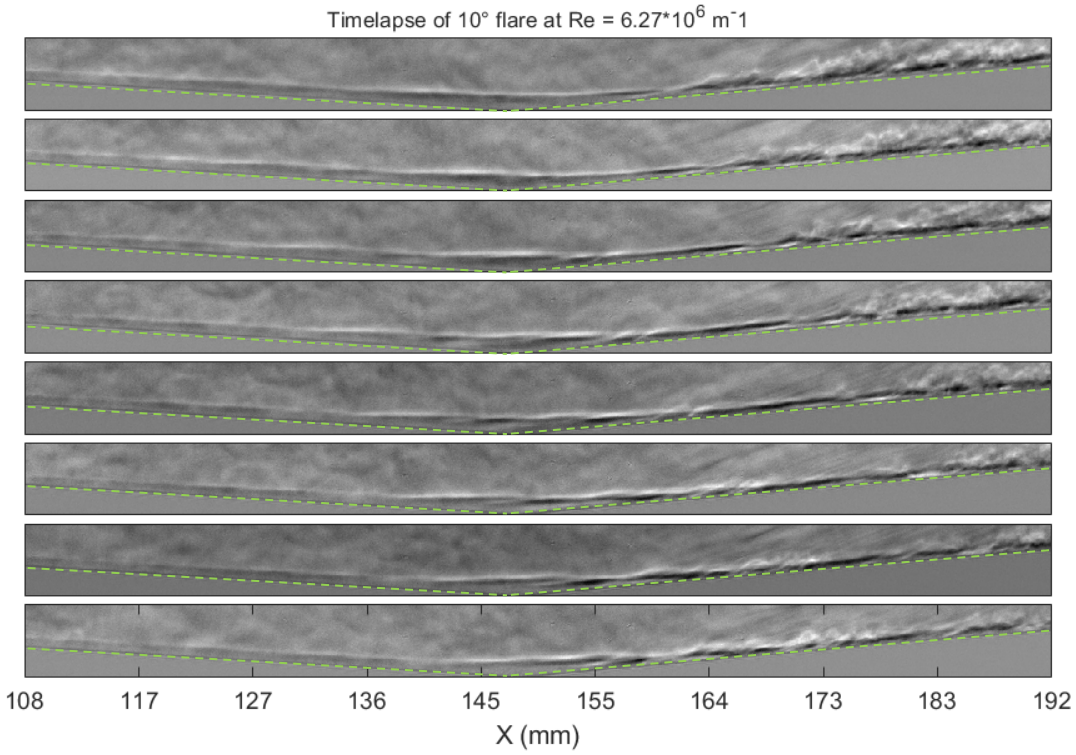

Figure 3.2: Background subtracted timelapse of +10° flare, images are 7.4 μs apart

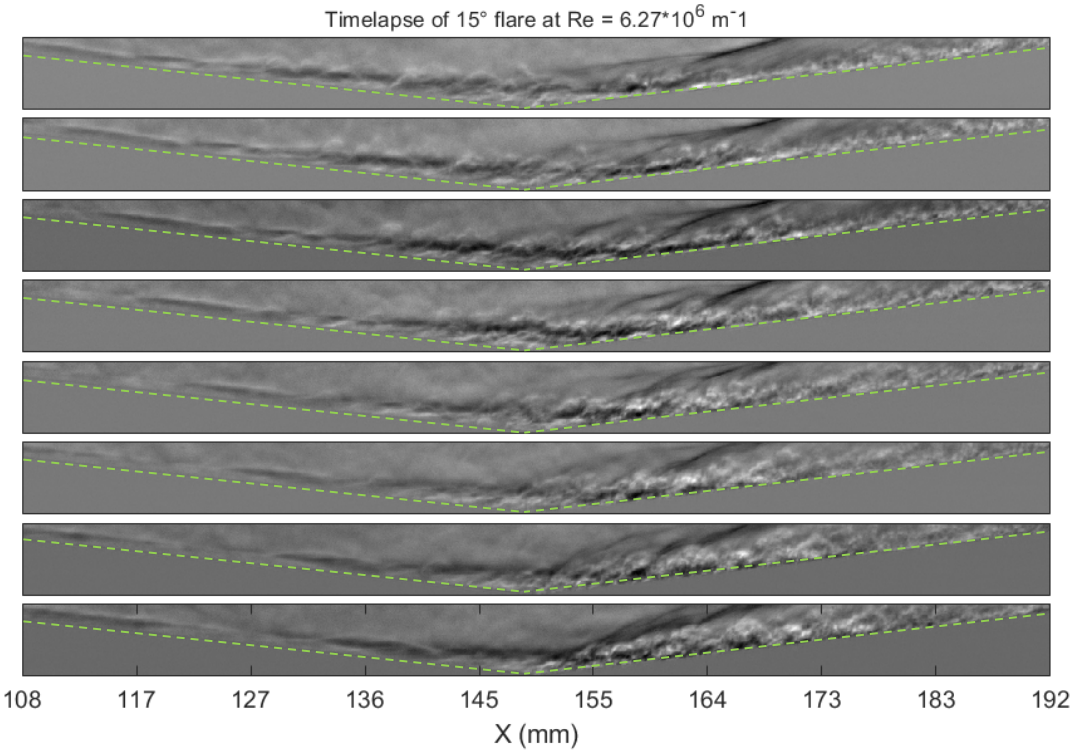

Figure 3.3: Background subtracted timelapse of +15° flare, images are 7.4 μs apart

In these image sequences the flow structures are easily recognizable, but further processing needs to be done to clearly see the first-mode wave packets. It is also clear in figure 3.1 and figure 3.2 that the flow remains attached through the compression corner for the +5° and +10° flare, while in figure 3.3 the flow has separated, and a reattachment shock is visible for the +15° flare between x = 155-164 mm. For all test cases shown the boundary layer is clearly visible and laminar along the cone surface and begins to transition to turbulence on the flare.

3.2 Power Spectral Density

Figure 3.4 highlights the difference in frequency content between the boundary layer, far upstream of the flare, and the freestream. The boundary layer exhibits a significant increase in all frequencies compared to freestream, but especially in the 10-60 kHz region. This increase is expected behavior of first-mode waves. Since these waves are travelling at an oblique angle to the camera their power content is weaker than when measuring second-mode waves.

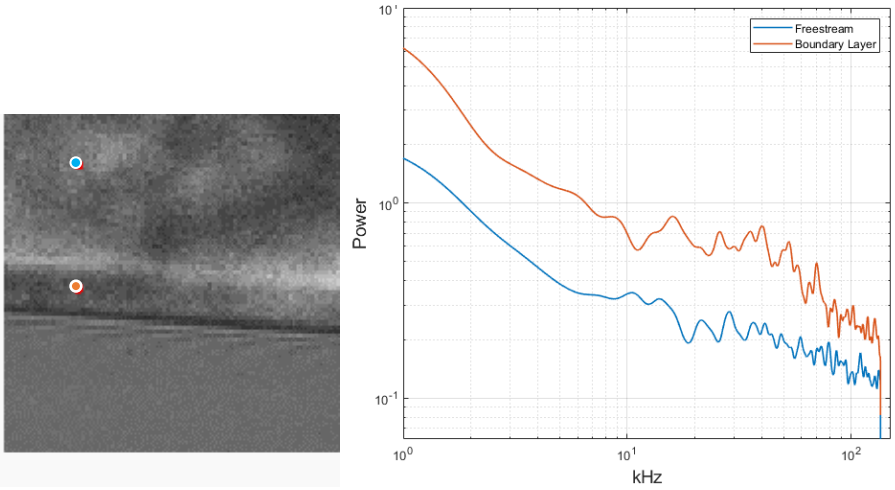

(a) (b)

Figure 3.4: The (a) colored dots are the locations for the corresponding (b) PSD results

The boundary layer PSD sampling locations are shown for the +5° flare in figure 3.5 with colors corresponding to the data represented in figure 3.6. For all three locations on the cone there is a significant increase in power from 10 to 60 kHz. This frequency content is consistent with first-mode waves. At the middle of the compression corner there is a less noticeable increase in power. For all locations on the flare the frequency content becomes more broadband as the boundary layer transitions to turbulence and any increase in power due to first-mode waves cannot easily be identified. The sampling location furthest forward on the flare has the highest overall power of all flare sampling locations, and energy decreases as the flow moves further along the flare. As expected, the turbulent boundary layer allows for energy to be dissipated at all frequencies, which explains this decrease in power.

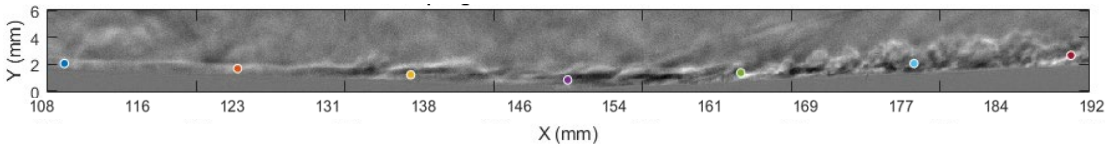

Figure 3.5: The colored dots are sampling locations for the PSD shown in fig 3.6

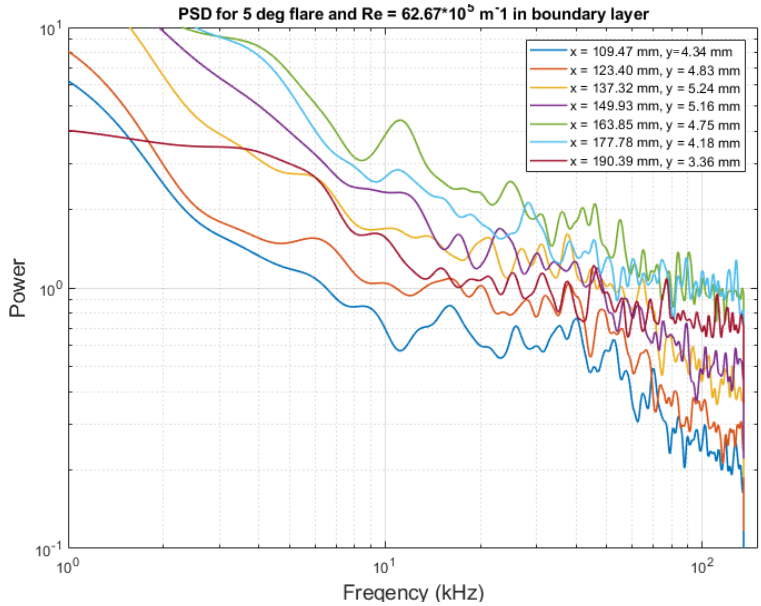

Figure 3.6: PSD for +5° flare at Re = 6.27

With the first-mode waves identified, a spatial PSD was computed by integrating the PSD over two frequency bands; 18 to 62 kHz, to capture as much of the first-mode frequency content as possible, and 20 to 40 kHz to highlight the frequencies with the largest increase in power. In figure 3.8 the strength of the integrated power in these frequency ranges can be seen increasing along the cone to a maximum just past the compression corner and then dissipating. The colormap scale is log10(PSD[20 kHz - 60kHz]). To highlight the 20 kHz - 40 kHz spatial PSD in figure 3.8 (b), a different scaled colormap was used as shown on the right side of the figure.

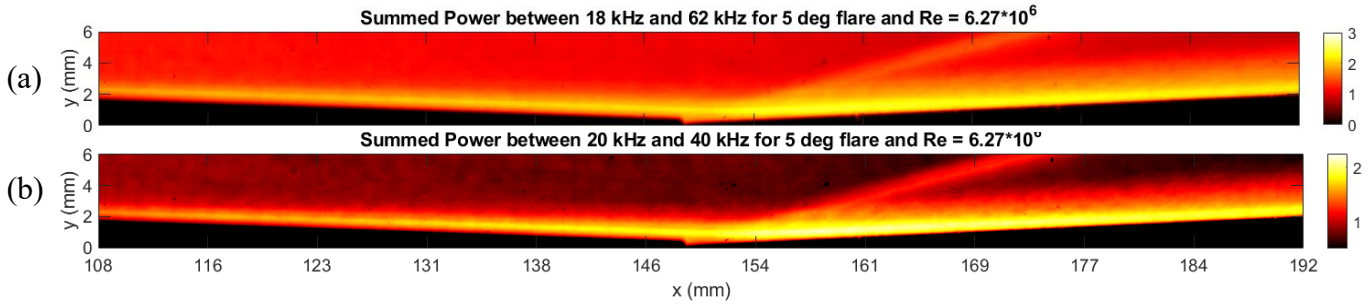

Figure 3.8: Spatial PSD for +5° flare between (a) 18 - 62 kHz and (b) 20 - 40 kHz

The +10° flare test shows many similarities to the +5° flare. In the background subtracted images, similar fluid structures are visible such as the laminar boundary layer along the cone forebody that transitions to turbulence on the flare. Also, the flow remains attached for both geometries. The PSD shown in figure 3.10 also exhibits many of the same attributes as the +5° flare. The 3 locations along the cone forebody show elevated frequency content between 10 - 60 kHz that grows in the downstream direction. The location at the compression corner and along the flare show elevated frequency content. The highest power content is seen at the location on the flare closest to the corner and then falls further downstream.

For the farthest downstream sampling location (x = 190 mm), there appears to be an increase in higher frequency content. This is due to aliasing of even higher frequency content in the turbulent boundary layer to the Nyquist limit of 135 kHz. This behavior was also identified at even higher frequency levels and at a higher Mach number in Sousa's work [22]

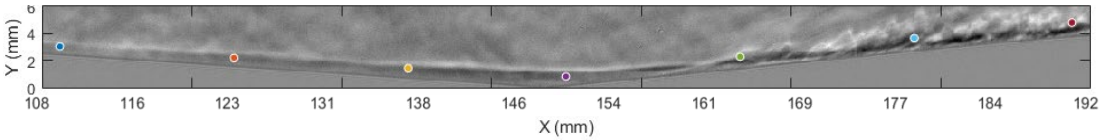

Figure 3.9: The colored dots are the sampling locations for the PSD in figure 3.10

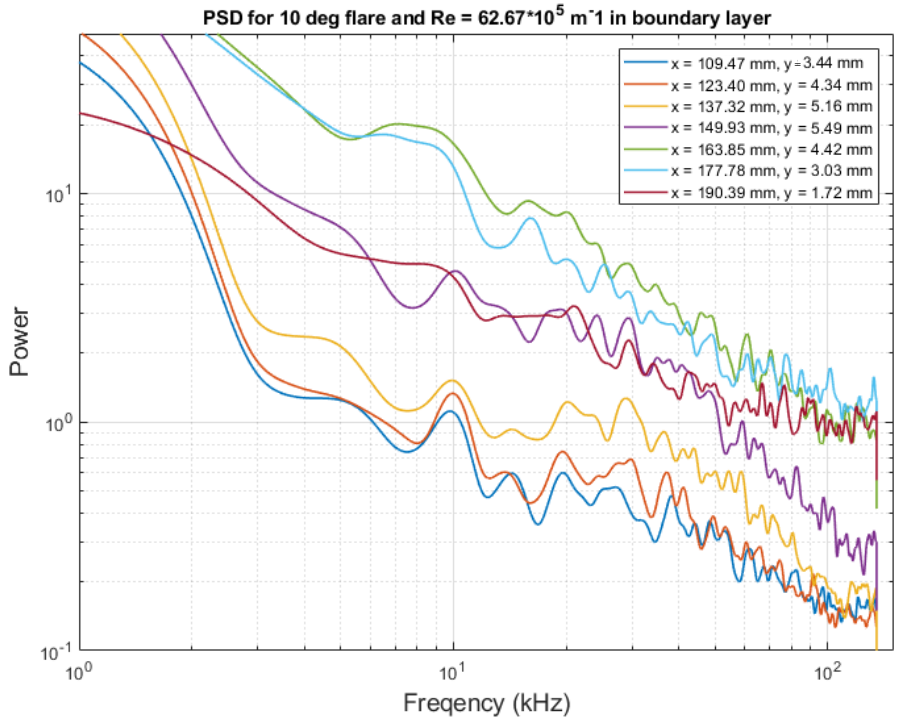

Figure 3.10: PSD for +10° flare at Re = 6.27

It is also worth noting that the 10 kHz peak seen in these PSD results is a tunnel artifact and is not related to first-mode waves or any other fluid structure. This artifact was first identified by Jones [31] and through SPOD is clearly visible in figure 3.11. The entire freestream and the model are shown to be a part of the frequency content which are both obviously not fluid structures. Additionally, the first-mode waves are

expected to be spread out over a range of frequencies below 100 kHz. The discrete increase in frequency at 10 kHz is further indication that it is not a result of fluid dynamics.

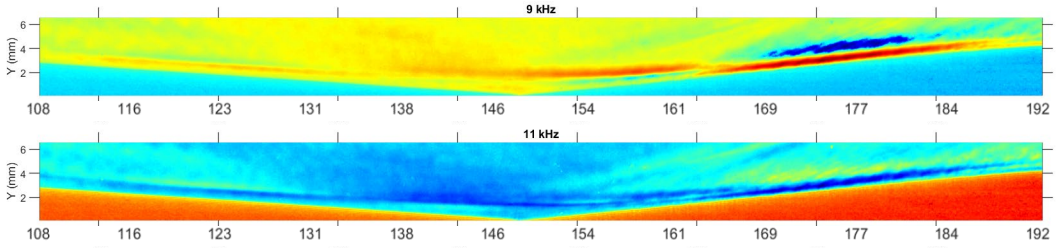

Figure 3.11: Visualization of SPOD Mode 1 around 10 kHz for the +10° flare; highlighting the tunnel artifact

The spatial PSD frequency range for all geometries was selected well above this artifact to isolate it from fluid structures. The +10° flare spatial PSD for 18-62 kHz and 20-40 kHz is presented in figure 3.12. Like the +5° flare the maximum power is located just behind the compression corner, although dissipation does not occur as quickly along the flare. The energy aligned with the flare shockwave is also not as prominent as in the +5° flare spatial PSD. At the corner (x = 150 mm) there appears to be a slight lift-off of energy, which could indicate the flow is slightly separated in this region.

(a)

(b)

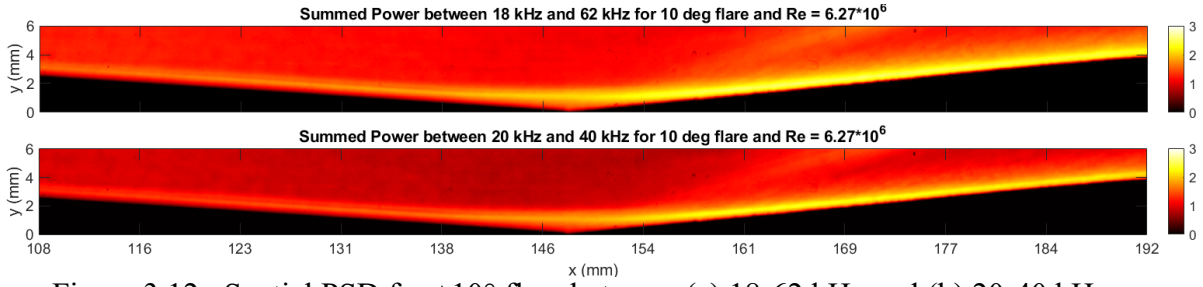

Figure 3.12: Spatial PSD for +10° flare between (a) 18-62 kHz and (b) 20-40 kHz

It is apparent in the background subtracted image of the +15° flare (figure 3.13) that the flow has separated as it encounters the compression corner, and a separation

bubble is observed at x = 150 mm. The sampling location had to be located significantly higher in the y-direction at this point to ensure the PSD was capturing the power of the shear layer and not lying within the separation bubble. Additionally, boundary layer transition for this flow condition oscillates between occurring along the cone body, as seen in figure 3.14 at x = 140 mm, and on the flare. Despite this, first-mode waves are clearly seen as elevated frequency content from 20 - 60 kHz in figure 3.14 for all cone sampling locations with a maximum between 20 and 40 kHz that grows in the downstream direction. The reattachment shock occurs around x = 160 mm, which also coincides with the highest measured power across all frequencies. The spectra of all high frequency content appear flatter which indicates rapid development of the turbulent boundary layer.

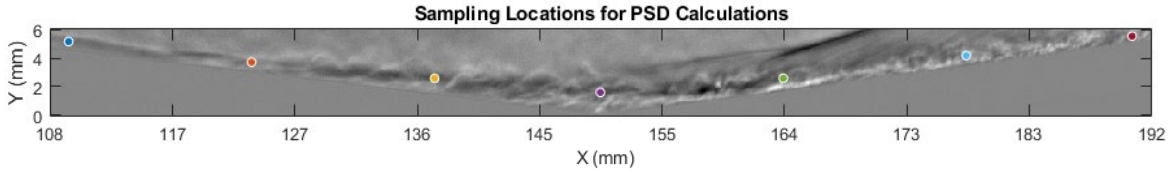

Figure 3.13: The colored dots are the sampling locations for the PSD in figure 3.14

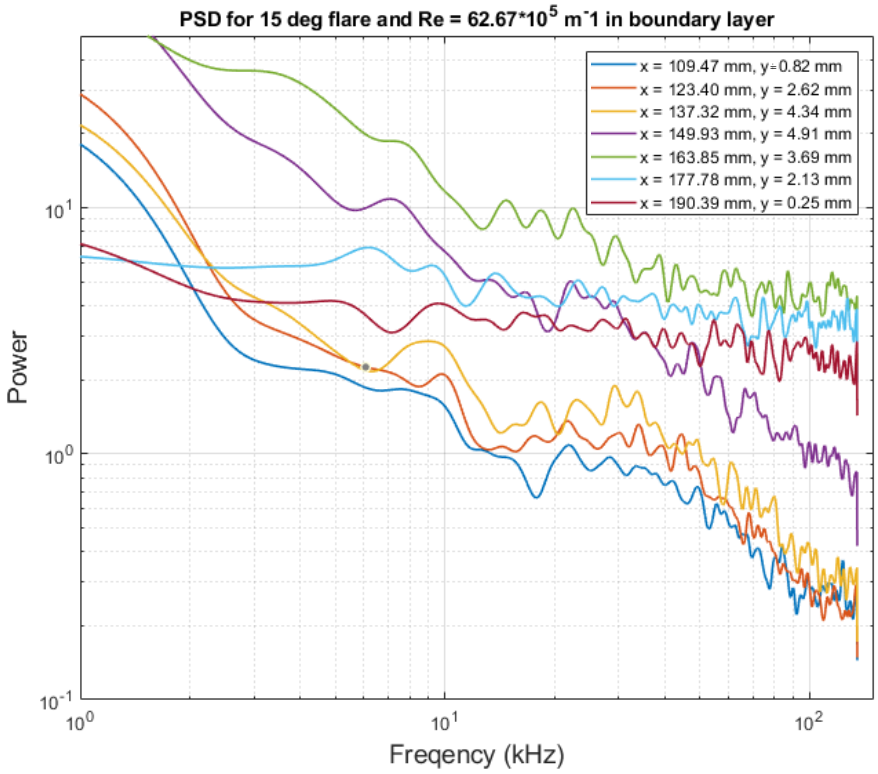

Figure 3.14: PSD for +15° flare at Re = 6.27

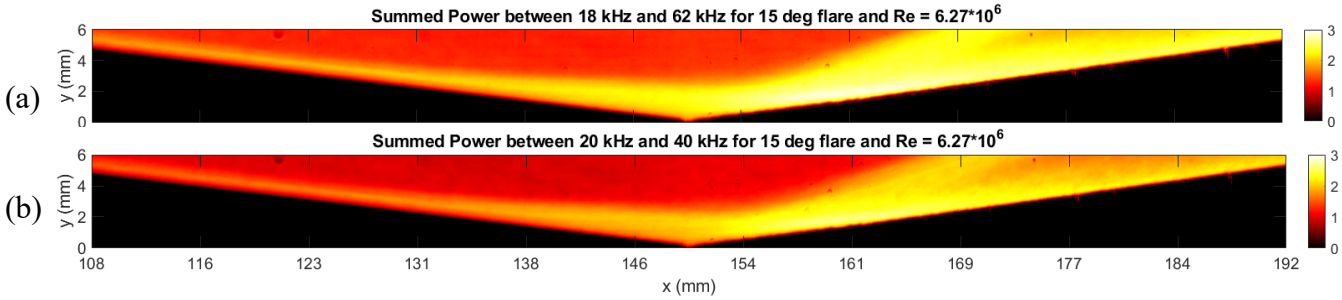

Figure 3.15: Spatial PSD for +15° flare between (a) 18 - 62 kHz and (b) 20 - 40 kHz

The spatial PSD presented in figure 3.15 helps visualize the flow separation as the region of increased power moves away from the cone-flare surface around x = 135 mm. The separation bubble is also seen as a region of decreased power compared to the shear layer at x = 150 mm. It also clearly visualizes the increase in power at the reattachment shock location at x = 161 mm, and the dissipation on the flare downstream.

3.3 Spectral Proper Orthogonal Decomposition

Despite the SPOD mode energies in figure 3.16 being taken for the entire image instead of discrete sampling locations, the increase in the energy due to first-mode waves is apparent from 20 - 60 kHz. Several frequencies in this range were visualized in figure 3.17 to highlight the interaction of the fluid structures with the cone-flare geometry.

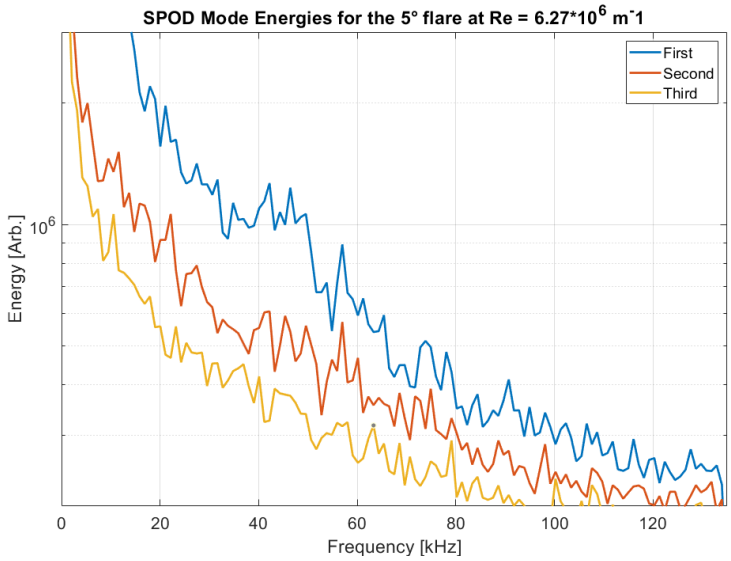

Figure 3.16: The first three SPOD mode energies across the frequency spectrum for the +5° flare

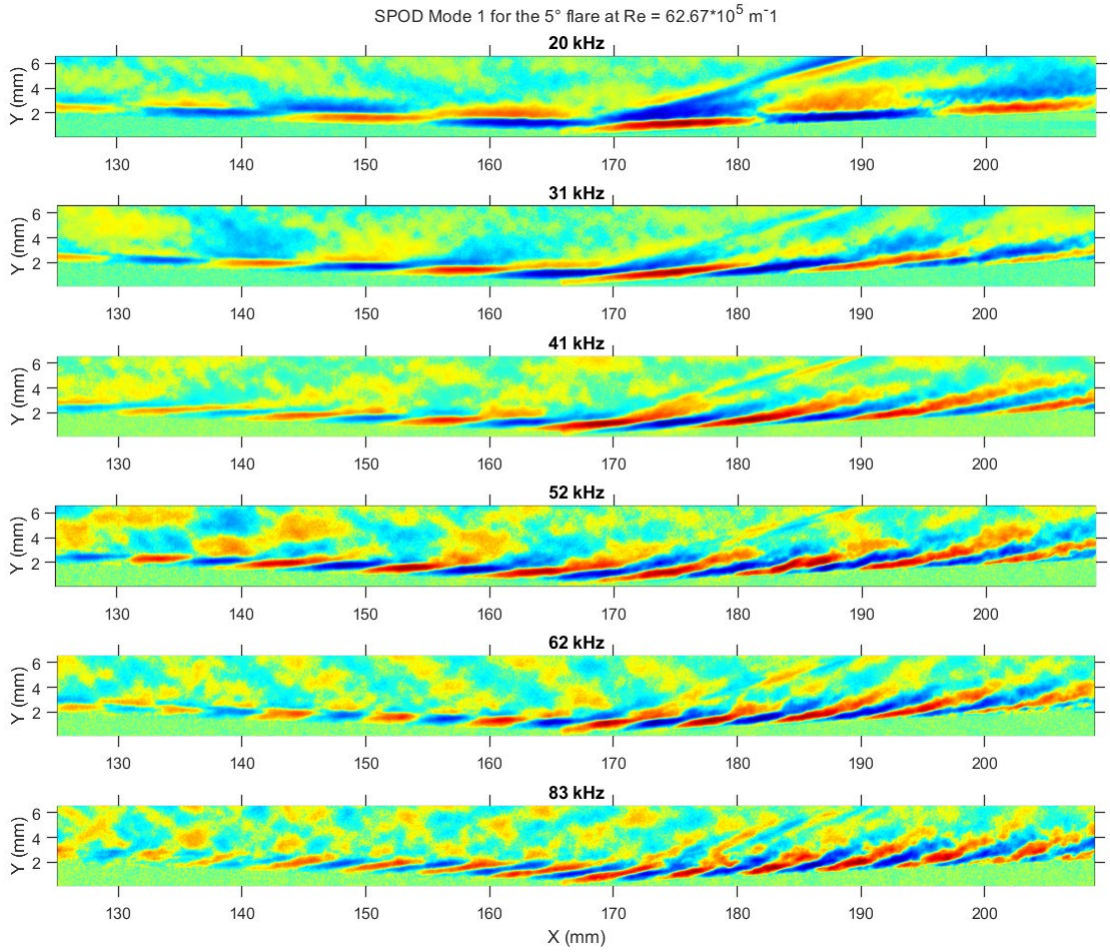

Figure 3.17: SPOD mode 1 visualization for the +5° flare at Re = 6.27 x10^6 m^{-1} for a range of frequencies

The selected frequencies for visualization are away from the 10 kHz artifact and span all the way to 83 kHz which would be a harmonic of the first-mode waves. The 62 kHz and 83 kHz frequencies appear to be harmonics of lower frequencies since they have similar structures but with half the wavelength. At 20 kHz there is a clear interaction between the disturbances and the flare shock wave that does not exist at any of the other frequencies. This indicates that some portion of the disturbance energy is being transmitted along the shock. At all frequencies, the first-mode wave packets within the boundary layer are clearly visible. Their growth along the cone surface is

quantified by the increase in their intensity. Their breakdown on the flare during boundary layer transition can also be observed by their intensity and coherence fading and the structures extending out further into the freestream.

For the +10° flare, the first-mode frequency content can be seen in elevated energy levels from 20-60 kHz in figure 3.18 from 20 kHz - 50 kHz. Also, the 10kHz tunnel artifact energy is extremely high and was visualized earlier in figure 3.11. The harmonics of this artifact could be contributing to the 30 kHz and 50 kHz local maxima.

Figure 3.18: The first three SPOD mode energies across the frequency spectrum for the +10° flare

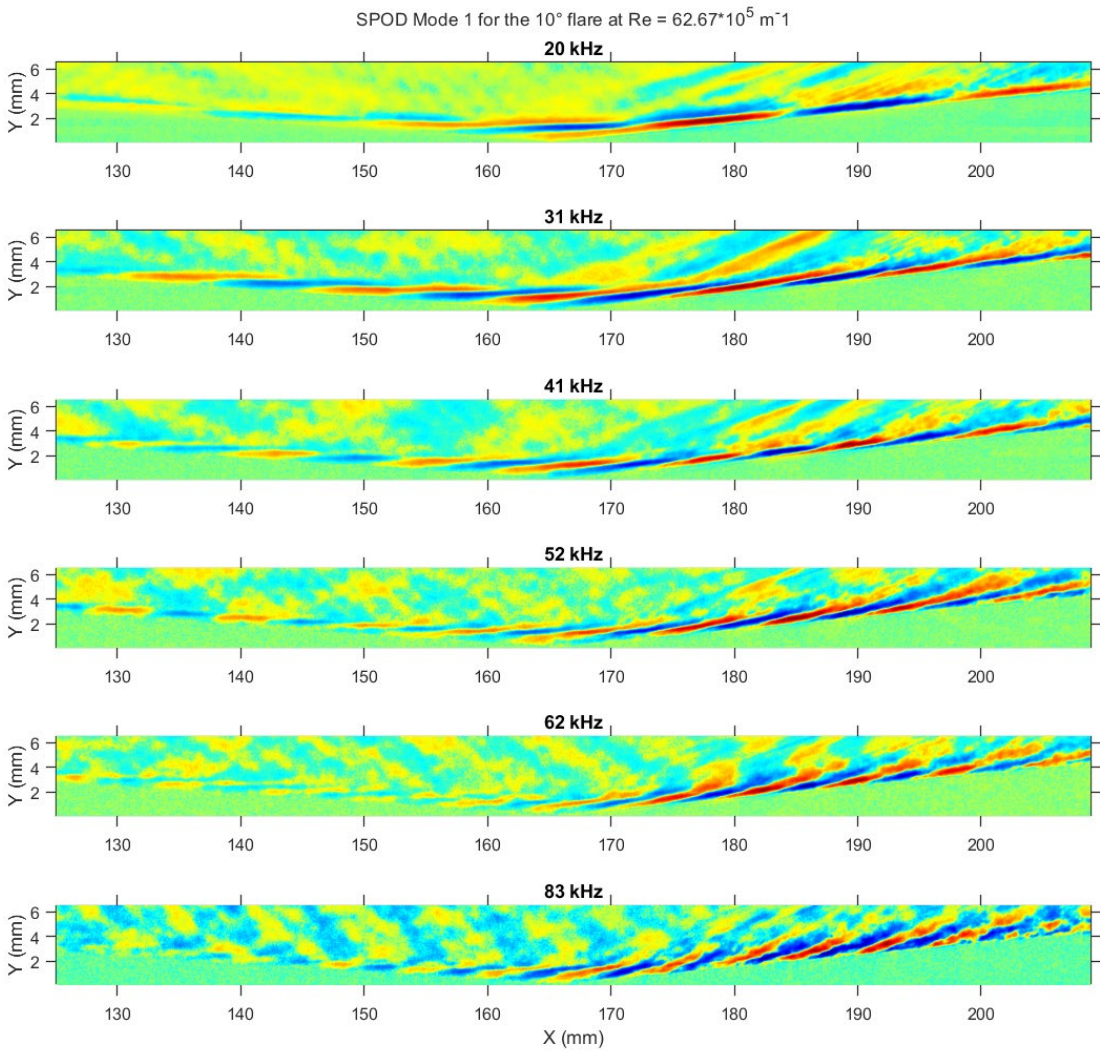

Figure 3.19: SPOD mode 1 visualization for the +10° flare at Re = 6.27 x10^6 m^{-1} for a range of frequencies

The elevated energy levels identified from figure 3.18 are confirmed in figure 3.19 as 31 kHz - 52 kHz have the most coherent and intense wave packets among the frequencies visualized. The wave packets at the other frequencies are not as well defined. The shock wave is no longer interacting with the wave packets at the 20 kHz frequency. However, a similar structure is emerging across the shock at the 31 kHz and 41 kHz frequencies but is separate from the structure seen in the +5° case since the intensity and wavelength are different from the boundary layer structures. This

structure can likely be attributed to Mach radiation. At the higher frequency cases of 62 kHz and 83 kHz it is clear the flare amplifies the wave packets much greater than at lower frequencies or at the lower +5° flare angle. The SPOD visualization in figure 3.19 reveals that harmonics of the 10 kHz tunnel artifact are likely not present since the intensity of the freestream and the model do not appear elevated.

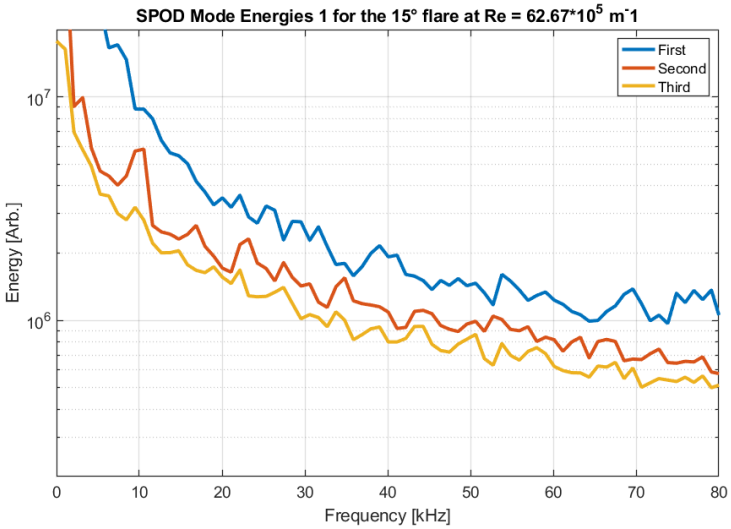

Figure 3.20: The first three SPOD mode energies across the frequency spectrum for the +15° flare

The first-mode frequency content is more difficult to discern in the SPOD mode energy spectrum for the +15° flare shown in figure 3.20. Higher frequency content appears to be dominating the energy spectrum. Elevated energy levels from 38 kHz to 52 kHz suggest that the frequency and power of the first-mode wave packets increase as flare angle increases.

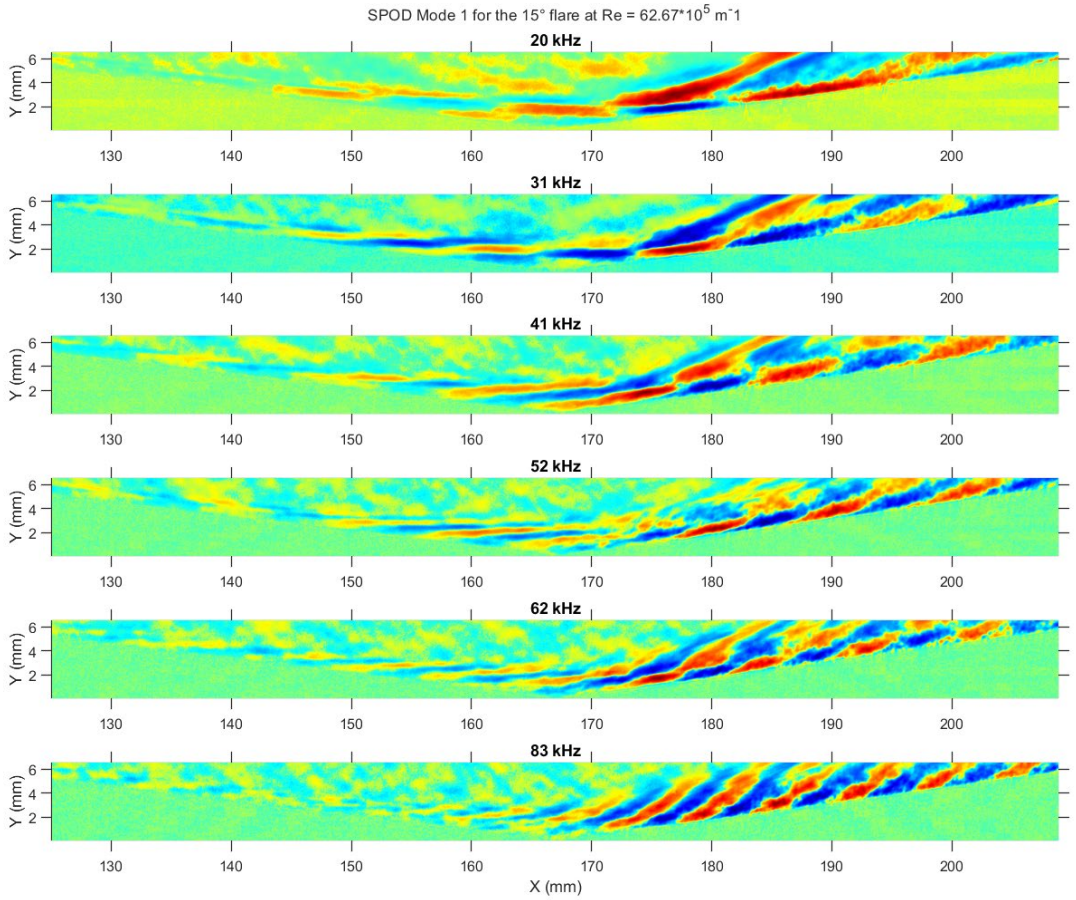

Figure 3.21: SPOD mode 1 visualization for the +15° flare at Re = 6.27 x10^6 m^{-1} for a range of frequencies

For the +15° flare, boundary layer wave packets along the flare were more amplified than in the other two geometries. Wave packets are most visible on the cone and the flare from 31 - 52 kHz. Further away from these frequencies the content is dominated by the turbulence on the flare. Interestingly, the reattachment shock is visible in the 20 - 40 kHz range, which suggests stronger Mach radiation from flow downstream of reattachment.

3.4 Bandpass Filtered Images

To confirm the accuracy of PSD and SPOD results, a Butterworth bandpass filter (10 - 40 kHz) was applied to the raw schlieren data, isolating first-mode waves. The filtered image was then reconstructed and advanced in time by 20 μs. This visualization also revealed first-mode wave packets traveling along the boundary layer and breaking up into turbulence. Additionally, the filtered data highlighted the shock wave at the same frequency as the wave packets, further suggesting an interaction between the shock wave and the first-mode waves. A single frame from the bandpass-filtered output is presented in the jet colormap in figure 3.22 for direct comparison to the SPOD visualization. A timelapse of the wave packets travelling along the cone-flare is shown in figure 3.23 with images 20 μs apart. In these images the wave packets can also be seen breaking apart and dissipating as the boundary layer transitions to turbulence.

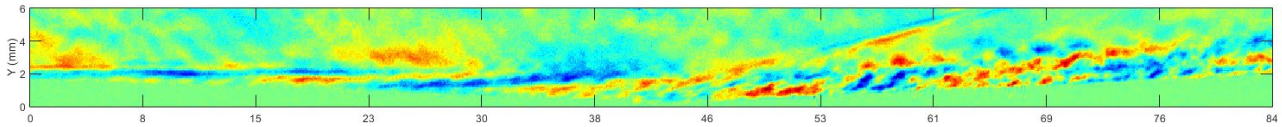

Figure 3.22: Bandpass filter (10 - 40kHz) for +5° flare in jet colormap for comparison to the SPOD figures.

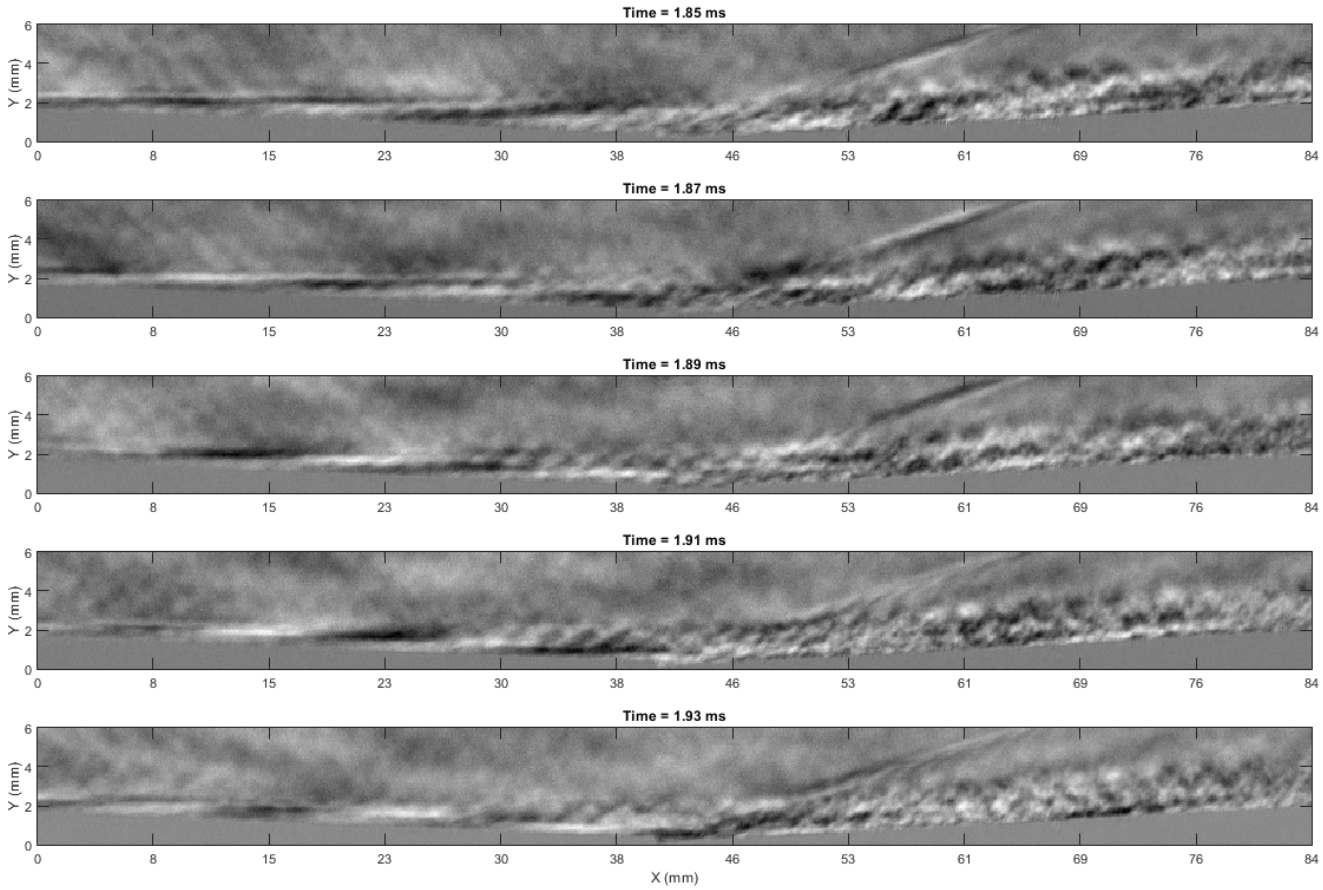

Figure 3.23: Butterworth bandpass filter (10 - 40 kHz) applied to a timeseries of raw images 20 μs apart of the +5° flare

3.5 Further Exploration of the +15° Flare

The high deflection angle of the +15° flare results in flow separation for all Reynolds numbers tested. While a Reynolds number of Re = 6.27 was useful for direct comparison of flow conditions for all flare angles, it also resulted in early transition of the boundary layer (visible in figure 3.13 at x = 130 mm), which reduces the window to identify first-mode wave packets. The PSD in figure 3.14 for the +15° flare Re = 6.27 does indicate the presence of first-mode waves, but the spatial PSD and the SPOD mode energies in figures 3.15 and 3.20 are dominated by the broadband spectrum of turbulence on the flare. Therefore, examining the +15° flare at a lower Reynolds number will give better visualization of the first-mode waves and will provide insight in how changing flow conditions affects where transition occurs.

For direct comparison of PSD results, the same y locations were sampled as shown in figure 3.13 and figure 3.24. It is also clear in figure 3.24 that for this lower Reynolds number the flow remains laminar along the cone surface for longer and transitions to turbulence on the flare.

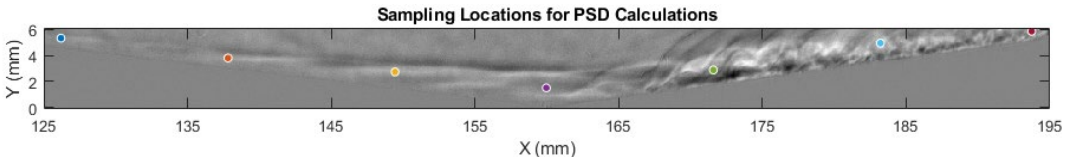

Figure 3.24: The colored dots are sampling locations for the PSD shown in figure 3.25

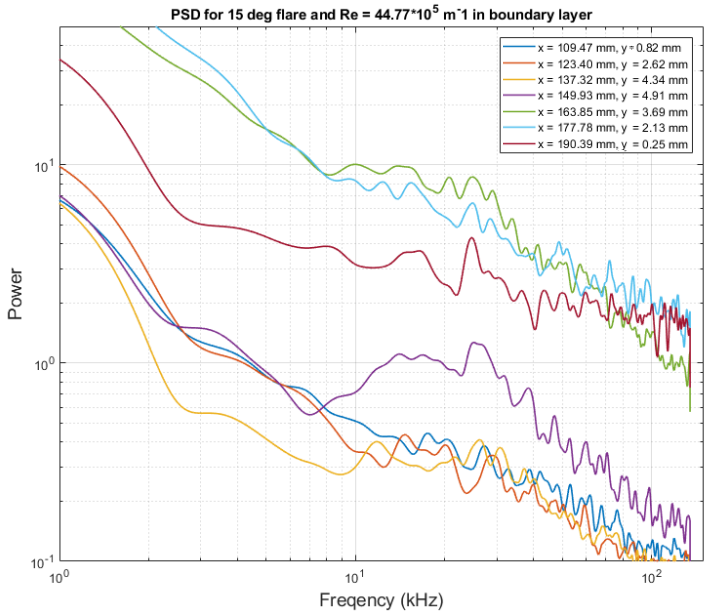

Figure 3.25: PSD for +15° flare at Re = 4.47 x 10^6 m^{-1}

An interesting result of the PSD shown in figure 3.25 is the substantial increase in content in the first-mode frequency range directly at the compression corner. This is likely due to the sampling location occurring within the shear layer between the boundary layer and the separation bubble. At x = 164 mm, just past the corner, there is increased first-mode frequency content (10 - 40 kHz). Since flow separates around the corner, the first-mode waves remain coherent onto the flare and through the reattachment shock. The first-mode waves appear to continue amplifying along the shear layer in contrast to the second mode waves studied in Butler & Laurence [23].

This theory is confirmed in the spatial PSD shown in figure 3.26. The first-mode content, specifically between 20 - 40 kHz continues to grow above the separation bubble until reattachment occurs along the flare. The substantial increase in strength of content within this frequency range at the compression corner seen in figure 3.25 is also confirmed by the spatial PSD. This could be a result of the separation bubble amplifying the first-mode waves. Shear layer disturbances, like first-mode waves, are

known to be vortical in nature. The viscous interactions of first-mode waves are increased when the laminar boundary layer flow separates from the wall and has a shear layer on both sides between the freestream and the separation bubble.

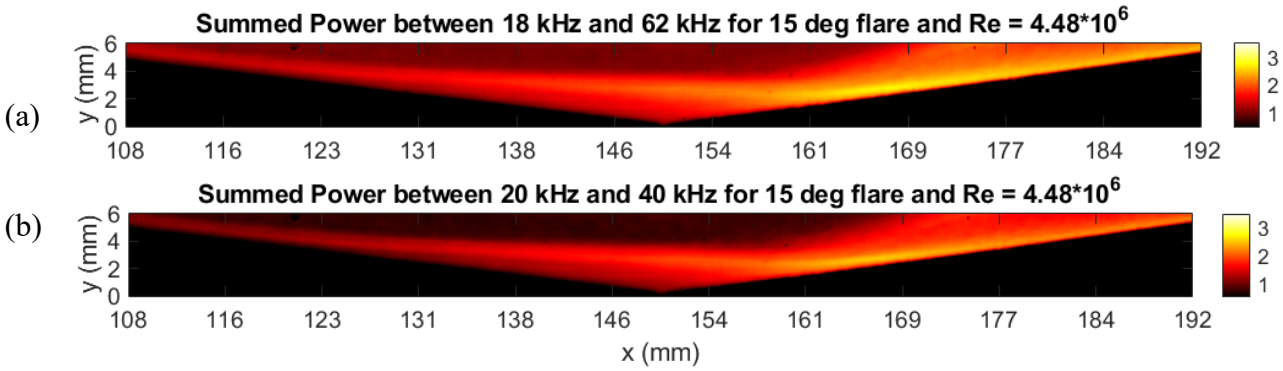

Figure 3.26: Spatial PSD for +15° flare between (a) 18 - 62 kHz and (b) 20 - 40 kHz at Re = 4.48 x 10^6 m^{-1}

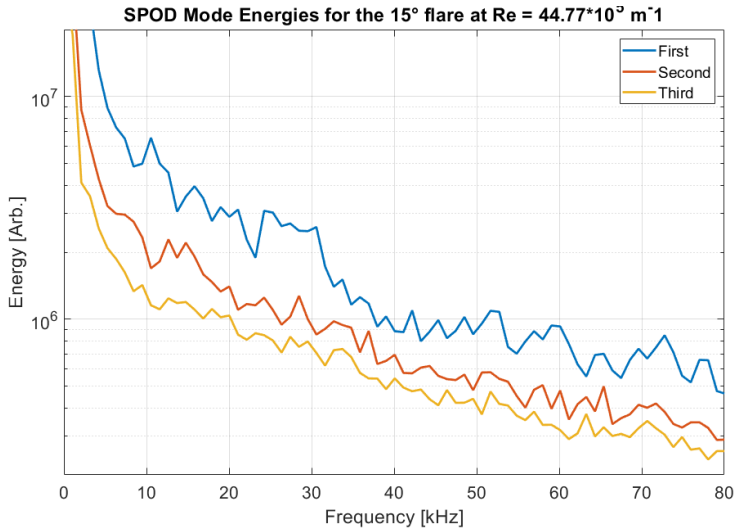

Figure 3.27: The first three SPOD mode energies across the frequency spectrum for the +15° flare at Re = 4.47 x 10^6 m^{-1}

The SPOD mode energies in figure 3.26 highlight the benefit of analyzing the lower Reynolds number. The first SPOD mode shows the first-mode frequency content between (10 - 40 kHz).

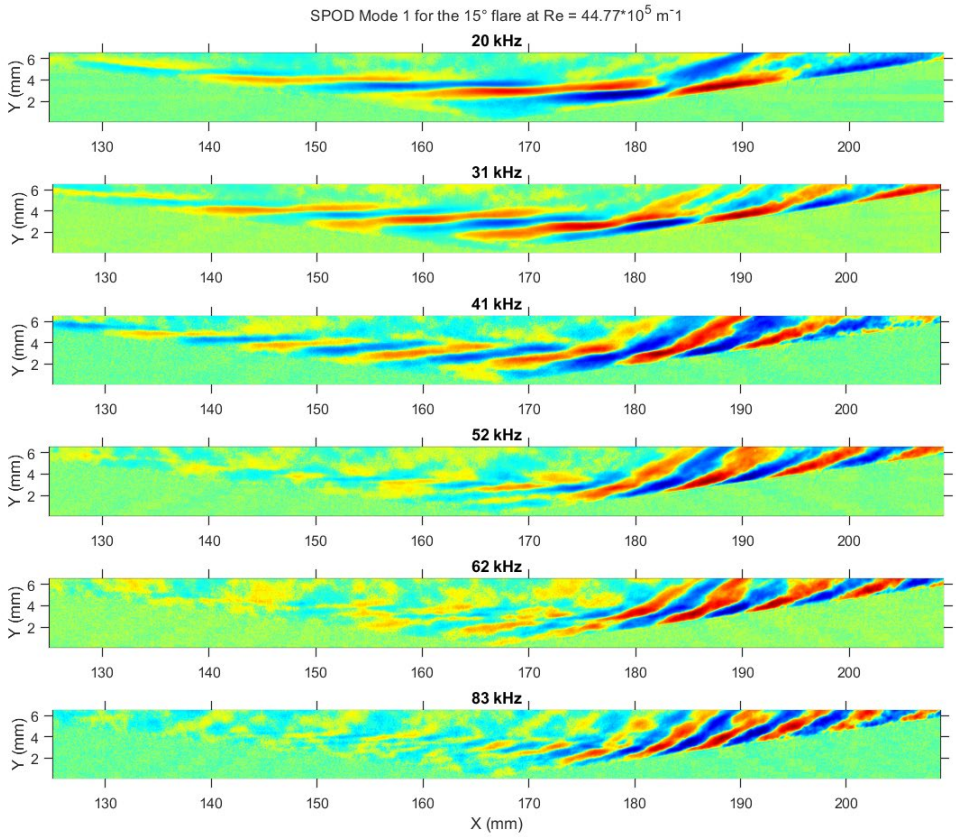

Figure 3.28: SPOD mode 1 visualization for the +15° flare at Re = 4.47 x10^6 m^{-1} for a range of frequencies

The SPOD visualization in figure 3.27 has much clearer flow structures than at the higher Reynolds number, especially at the lower frequencies. This visualization also confirms that the waves are traveling above and are amplified by the separation bubble, before quickly breaking down to turbulence following reattachment.

Chapter 4: Conclusion

4.1 Summary of Results

This study explored the behavior of first-mode instability waves in Mach 4 flow over cones with varying flare angles. The key goal was to understand how these waves contribute to the transition of the boundary layer from a laminar to a turbulent state and the impact the cone-flare geometry plays in this transition. As flare angle increased the first-mode waves broke down sooner within the flow for the same flow conditions. The first mode waves broke down the quickest when the flow separated, as on the +15° flare, and when transition was occurring before the flare at higher Reynolds numbers.

Power Spectral Density (PSD) analysis revealed a characteristic frequency range (10 - 60 kHz) associated with first-mode waves within the boundary layer. This wave activity intensified along the cone surface, peaked near the compression corner, and then weakened as the flow transitioned to turbulence on the flare.

Spectral Proper Orthogonal Decomposition (SPOD) provided further insights by isolating coherent flow structures and their energy distribution. SPOD visualizations confirmed the presence and development of first-mode waves, along with their eventual breakdown on the flare. The analysis also suggested an interaction between the first-mode waves and the corner or reattachment shock wave in certain flow conditions.

Finally, applying a bandpass filter to the raw images provided additional insight into the spatiotemporal characteristics of the first-mode wave packets in the boundary layer and their breakdown during transition to turbulence. The amplification and rapid

breakdown of first-mode waves across the separated shear layer indicates that avoiding separation is crucial when first-mode waves are dominant if early transition is to be avoided. These findings offer valuable insight into the frequency, power, and influence of first-mode waves on boundary layer transition on the cone-flare geometry.

4.2 Future Work

The work presented characterizes how first-mode waves influence boundary layer transition for a variety of cone-flare geometries without the introduction of aerosols or droplets within the flow. Since the test facility, MIST, has the capability to load the working fluid with aerosols or droplets, a follow-up study could compare the results presented here with similar tests with aerosols or droplets. This would allow for characterization of how the propagation of the first-mode changes in the presence of aerosols or droplets that would typically be seen in a hypersonic vehicle's flight regime, offering insights into real-world flight conditions.

Additionally, while the work presented focused primarily on the first-mode, further work could study how the second-mode propagates within the boundary layer for these geometries. This would require minor modifications to the test setup to allow for higher sampling rates but would enable a more direct comparison to the extensive body of research performed at higher Mach numbers. It would also be beneficial to increase the Mach number to around Mach 5 where the second-mode is more prevalent, but the first-mode still exists.

Appendices

MATLAB code developed for data analysis:

PSD, SPOD, & Bandpass Filtering

```
clear
clc
mm_pix = 0.081896; %Pixel Scale mm/pixel
flare_angle = input('Enter the flare angle (in degrees): ');
x_le = 108; %% leading edge of x is at 108 mm

% Prompt the user to input the charge tube pressure
charge_pressure = input('Enter the charge tube pressure (in bar): ');

[Ma,Re]=MISTfreestream_userInput(charge_pressure,296);

shot = 1;
directory_path = uigetdir('C:\', 'Select Directory containing TIFF
images');
if directory_path == 0
    error('Operation canceled by user.');
end
shot = 1;
imageDir=directory_path;
fr = 270000;
% Get a list of all TIFF files in the directory
tiff_files = dir(fullfile(directory_path, '*.tif'));

% Initialize an empty 3D matrix to store the image data
num_files = numel(tiff_files);
first_image = imread(fullfile(directory_path, tiff_files(1).name));
[height, width] = size(first_image);
P = zeros(height, width, num_files, 'double');

% Loop through each TIFF file and load it into the matrix
for i = 1:num_files
    file_path = fullfile(directory_path, tiff_files(i).name);
    P(:,:,i) = imread(file_path);
end
P=flip(P,2);
P=flip(P,1);
% Display the first image (optional)
figure(1);
```

```
imshow(P(:,:,1000), []);
title('First Image');
```

PSD for user selected area

```
frame_data=P(:,:,1000);
frame_rate=fr;
% Display the frame
imshow(frame_data, []);
bg = mean(P,3);
D = (P-bg);
imshow(D(:,:,1000), []);

% Prompt the user to select a point
disp('Please click on the image to select a point for analysis.');
[x, y] = ginput(1);
x = round(x);
y = round(y);
```

Background Subtraction Visualization

```
startFrame = 1000;
startTime = 1000/fr;
frameStep = 2;  % Interval of frames
numImagesToShow = 8;  % Number of images to show

% Create a figure and use a tiled layout
figure;

tiledlayout(numImagesToShow, 1,'TileSpacing','compact');  % 1 row,
numImagesToShow columns
% Loop through the desired frames
for i = 0:numImagesToShow - 1
    % Calculate the frame index
    frameIndex = startFrame + i * frameStep;

    % Check if the frame index exceeds the number of frames
    if frameIndex > size(D, 3)
```

```
        disp(['Frame index ' num2str(frameIndex) ' exceeds the number
of frames.']);
        break;
    end

    % Select the tile and display the image using imagesc
    ax = nexttile;

    imagesc(D(:,:,frameIndex));
    axis tight
    %title(sprintf('Time = %0.2f ms', (frameIndex/fr)*1e3));
    %colorbar;  % Add a color bar to each subplot to show the scaling
of values

    % Get the size of the current image
    [imgHeight, imgWidth] = size(D(:,:,frameIndex));

 yticks([])
 xticks([])
    % Adjust color map and scaling
    colormap(ax, gray);  % Set color map to 'jet'
    %set(ax, 'Layer', 'top');  % Ensure the axes ticks and labels are
on top of the image
    hold on
 end
 xticks(ax, linspace(1, imgWidth, 10));  % Set ticks every 10 mm
 xtick_string = round(x_le:(round(x_le+1024*mm_pix)-
x_le)/9:round(x_le+1024*mm_pix))';
 xtick_string = num2str(xtick_string);
 xticklabels(ax, xtick_string);
 set(ax,"FontSize",14)
    xlabel(ax, 'X (mm)');
    title_txt= sprintf('Timelapse of %d%c flare at Re = %0.2f*10^6 m^-
1',flare_angle,char(176),Re/10^6);
    sgtitle(title_txt)
```

PSD Point Selection

```
 %Point Selection
 x =  [18 188 188+170 512 512+170 512+340 1024-18];
 y(1) = 9;
 y(2) = 26;
 y(3) = 40;
 y(4) = 55;
```

```
 y(5) = 43;
 y(6) = 21;
 y(7) = 5;

 x_real = x.*mm_pix;
 y_real = y.*mm_pix;
 figure;
 % Display the image using imagesc
 imagesc(D(:,:,1000));
 colormap gray;  % Set the colormap to gray (if the image is grayscale)
 axis equal tight;  % Keep the aspect ratio and fit the axes to the
image
 hold on;

 % Plot the points on the image
 plot(x(1), y(1), 'Marker','o','MarkerFaceColor','#0072BD',
'MarkerEdgeColor','w','MarkerSize', 5);
 plot(x(2), y(2), 'Marker','o','MarkerFaceColor','#D95319',
'MarkerEdgeColor','w','MarkerSize', 5);
 plot(x(3), y(3), 'Marker','o','MarkerFaceColor','#EDB120',
'MarkerEdgeColor','w','MarkerSize', 5);
 plot(x(4), y(4), 'Marker','o','MarkerFaceColor','#7E2F8E',
'MarkerEdgeColor','w','MarkerSize', 5);
 plot(x(5), y(5), 'Marker','o','MarkerFaceColor','#77AC30',
'MarkerEdgeColor','w','MarkerSize', 5);
 plot(x(6), y(6), 'Marker','o','MarkerFaceColor','#4DBEEE',
'MarkerEdgeColor','w','MarkerSize', 5);
 plot(x(7), y(7), 'Marker','o','MarkerFaceColor','#A2142F',
'MarkerEdgeColor','w','MarkerSize', 5);
 % Customize axes to reflect millimeter scale
 ax = gca;  % Get current axes
 imgHeight = size(D, 1);
 imgWidth = size(D, 2);

 % Set the x and y ticks to show the scale in millimeters
 xticks(ax, linspace(1, imgWidth, 10));  % Set ticks every 10 mm
 yticks(ax, linspace(1, imgHeight, 4)); % Set ticks across the height
 % Label the ticks in millimeters
 xtick_string = round(x_le:(round(x_le+1024*mm_pix)-
x_le)/9:round(x_le+1024*mm_pix))';
 xtick_string = num2str(xtick_string);
 xticklabels(ax, xtick_string);
 yticklabels(ax, flip(round(linspace(0, (imgHeight-1)*mm_pix, 4))));

 % Set labels for the axes
```

```
xlabel('X (mm)');
ylabel('Y (mm)');

% Set the title
title('Sampling Locations for PSD Calculations');

% Ensure the plot elements are visible over the image
set(ax, 'Layer', 'top');
hold off;
```

PSD Calculation

```
figure;
psdFig = zeros(1,length(x));
legendString = cell(1,length(x));
for i = 1:length(x)
    region = [y(i)-1:y(i)+1;x(i)-1:x(i)+1];
    P_signal = zeros(3, 3, size(D, 3));
    bins=32;
    for k = 1:3
        for j = 1:3
            % Extract the 3x3 region for the current frame
            P_signal = D(region(1,j),region(2,k), :);
            P_signal = squeeze(P_signal);
            seglength=round(length(P_signal)/bins);

[Pxx(:,j,k),Fxx]=pwelch(P_signal,hamming(seglength),[],2^12,fr);
        end
    end
    Pxxavg=sum(Pxx,2)/length(size(D,3));
    Pxxavg2=sum(Pxxavg,3)/length(size(D,3));
    if i == 1
        Pxxavg_boundarylayer = Pxxavg2;
    end
    psdFig(i) = loglog(Fxx/1e3, Pxxavg2, 'LineWidth', 1.2);
    xlabel('Freqency (kHz)', 'FontSize', 14);
    ylabel('Power', 'FontSize', 14);
    title_string = sprintf('PSD for %d deg flare and Re = %0.2f*10^5
m^-1 in boundary layer', flare_angle, Re/10^5);
    title(title_string);
    xlim([1 150])
    ylim([0.1 50])
    grid on;
    hold on
```

```
    legendString{i} = sprintf('x = %0.2f mm, y = %0.2f
mm',x_real(i),y_real(i));
 end
 legend(legendString)
 hold off
```

Spatial PSD

```
 %clear Pxx_spatial
 %clear Fxx_spatial
 figure;
    P_signal = zeros(size(P,1),size(P,2), size(D, 3));
    Pxx_spatial = zeros(size(P,1),size(P,2), 2049);
    Fxx_spatial = zeros(size(P,1),size(P,2), 2049);
    bins=32;
    for k = 1:size(P,1)
        for j = 1:size(P,2)
            P_signal = D(k,j,:);
            P_signal = squeeze(P_signal);
            seglength=round(length(P_signal)/bins);
            [Pxx,Fxx]=pwelch(P_signal,hamming(seglength),[],2^12,fr);
        Pxx_spatial(k, j, :) = Pxx;
        Fxx_spatial(k, j, :) = Fxx;
        end
    end
```

Visualizing Spatial PSD

```
 mm_pix = 0.081896;
 clear power_sum
 imgWidth = size(D,2);
 imgHeight = size(D,1);
 % Define frequency range
 freq_low = 9000;  % 10 kHz
 freq_high =40000;   % 60 kHz

 % Initialize matrix to store summed power
 power_sum = zeros(size(D, 1), size(D, 2));

 % Find indices corresponding to the desired frequency range
```

```
 % 'squeeze' is used to collapse the first frequency vector, assuming
frequency response is the same for all pixels
 freq_indices = find(Fxx_spatial(1, 1, :) >= freq_low & Fxx_spatial(1,
1, :) <= freq_high);

 % Sum powers across the specified frequency range for each pixel
 for k = 1:size(D, 1)
     for j = 1:size(D, 2)
         % Sum PSD values over the range for each pixel
         power_sum(k, j) = sum(Pxx_spatial(k, j, freq_indices));
     end
 end

 power_sum=flip(power_sum,1);
 log_power_sum = log10(power_sum);
 % Assuming 'power_sum' is already computed
 log_power_sum(log_power_sum <=0) = 0;
 figure;
 h = contourf(log_power_sum, 256,'LineStyle','none'); % Use more levels
for smoother gradients
 colorbar;

 % Adjust colormap: prepend black to the 'jet' colormap for the
marker_value
 custom_colormap = [0 0 0; hot(256)]; % Black followed by 64 colors
from jet
 clim([0.5 3.5])
 colormap(custom_colormap);

 % Add labels and title
 title('Logarithm of Summed Power between 10 kHz and 60 kHz, with Non-
Positive Values in Black');
 xlabel('Pixel Column Index');
 ylabel('Pixel Row Index');
 titlestring = sprintf('Summed Power between %d kHz and %d kHz for %d
deg flare and Re =
%0.2f*10^6',freq_low/1000,freq_high/1000,flare_angle, Re/10^6); % Add a
title to the plot
 title(titlestring)
 axis equal
     xticks(linspace(1, imgWidth, 12));  % Set ticks across the width
     yticks(linspace(1, imgHeight, 4)); % Set ticks across the height

     % Label the ticks in millimeters
     xticklabels(round(linspace(x_le, x_le+(imgWidth-1)*mm_pix, 12)));
```

```
    yticklabels((round(linspace(0, (imgHeight-1)*mm_pix, 4))));
ax = gca;
set(ax,'FontSize',14)
xlabel('x (mm)'); % Label x-axis
ylabel('y (mm)'); % Label y-axis
```

Freestream PSD

```
x_freestream = x(3);
y_freestream = 31;
x_real_freestream = x_freestream*mm_pix;
y_real_freestream = y_freestream*mm_pix;

%Show where PSD is being taken in freestream vs boundary layer
figure;
imshow(D(:,:,1000), []);
hold on
plot(x_freestream,y_freestream,'r.','MarkerSize',9);
plot(x(1),y(1),'r.','MarkerSize',9)
hold off

% Extract a 3x3 region around the selected point
region_freestream = [y_freestream-1:y_freestream+1;x_freestream-
1:x_freestream+1];
P_signal_freestream = zeros(3, 3, size(D, 3));
bins =32;
for k = 1:3
    for j = 1:3
        % Extract the 3x3 region for the current frame
        P_signal_freestream =
D(region_freestream(1,j),region_freestream(2,k), :);
        P_signal_freestream = squeeze(P_signal_freestream);
        seglength_freestream=round(length(P_signal_freestream)/bins);

[Pxx(:,j,k),Fxx]=pwelch(P_signal_freestream,hamming(seglength_freestrea
m),[],2^12,fr);
    end
end
Pxxavg=sum(Pxx,2)/length(size(D,3));
Pxxavg2_freestream=sum(Pxx,3)/length(size(D,3));
Pxxavg3_freestream=sum(Pxxavg2_freestream,2)/length(size(D,3));

%Freestream vs Boundary Layer
```

```
 figure;
 loglog(Fxx/1e3, Pxxavg3_freestream, 'LineWidth', 1.2);
 hold on
 loglog(Fxx/1e3, Pxxavg_boundarylayer, 'LineWidth', 1.2);
 xlabel('kHz', 'FontSize', 14);
 ylabel('Power', 'FontSize', 14);
 title_string = sprintf('PSD for %d deg flare and Re = %0.2f*10^5 in
freestream vs boundary layer', flare_angle, Re/10^5);
 title(title_string);
 grid on;
 xlim([1 150])
 legend('Freestream','Boundary Layer')

 %Absolute Difference
 figure;
 loglog(Fxx/1e3, abs(Pxxavg3_freestream-Pxxavg_boundarylayer),
'LineWidth', 1.2);
 xlabel('kHz', 'FontSize', 14);
 ylabel('Power', 'FontSize', 14);
 title_string = sprintf('Difference in PSD for %d deg flare and Re =
%0.2f *10^6 between boundary layer and freestream', flare_angle,
Re/10^6);
 title(title_string);
 grid on;
 xlim([1 150])
 ylim([10^-2 10^1])

 %RMS
 Pxxavg_freestream_RMS=Pxxavg3_freestream/rms(Pxxavg3_freestream);
 Pxxavg_RMS=Pxxavg_boundarylayer/rms(Pxxavg_boundarylayer);
 Pxx_RMS_diff = abs(Pxxavg_freestream_RMS-Pxxavg_RMS);
 Pxx_RMS_diff_movmean = movmean(Pxx_RMS_diff,75);
 Pxx_RMS_diff_smooth = smoothdata(Pxx_RMS_diff);

 figure;
 loglog(Fxx/1e3,Pxxavg_freestream_RMS,'LineWidth', 1.2)
 hold on
 loglog(Fxx/1e3,Pxxavg_RMS,'LineWidth', 1.2)
 xlabel('kHz', 'FontSize', 14);
 ylabel('Power', 'FontSize', 14);
 xlim([1 150])
 ylim([10^-1 10^1])
 title('RMS difference in freestream vs boundary layer')
 legend('Freestream','Boundary Layer')
 grid on
```

```
 %Normalized
 Pxx_normalized_freestream =
smoothdata(normalize(Pxxavg3_freestream,"range"));
 Pxx_normalized=smoothdata(normalize(Pxxavg_boundarylayer,"range"));
 figure;
 loglog(Fxx/1e3,Pxx_normalized_freestream,Fxx/1e3,Pxx_normalized,'LineW
idth', 1.2)
 xlabel('kHz', 'FontSize', 14);
 ylabel('Power', 'FontSize', 14);
 xlim([1 150])
 ylim([0 1])
 title('Normalized difference in freestream vs boundary layer')
 legend('Freestream','Boundary Layer')
 grid on
```

SPOD

```
 % Crop the image to a specific range of y pixels
 y_start = 1; % Specify the starting y pixel
 y_end = 80;   % Specify the ending y pixel
 P_cropped = P(y_start:y_end, :, :);
 [num_rows, num_cols, num_frames] = size(P_cropped);

 % Define the window parameters
 window_length = 256; % Specify the window length
 window = hamming(window_length); % Use a Hamming window
 P_cropped_transpose = permute(P_cropped,[3 1 2]);
 P_cropped_transpose_flipped =
P_cropped_transpose;%flip(P_cropped_transpose,2);
 [L, Pout, f] = spod(P_cropped_transpose_flipped, window,[],[],1/fr);
%cropped
```

Plot the Eigenvalue Spectrum Jet Colormap

```
 figure; clf;
 cscale = linspace(0, 1, size(L, 2));
 %cmap = jet(size(L, 2));  % Get colormap values

 for ii = 1:3%size(L, 2)
```

```
    semilogy(f/1000, L(:, ii), 'LineWidth',2)
    if ii == 1
        hold on
    end
end
hold off
grid on
xlabel('Frequency [kHz]'), ylabel('Energy [Arb.]')
set(gca, 'FontSize', 16)
xlim([0 max(f)/1000])
legend('First','Second','Third')
    title_txt= sprintf('SPOD Mode Energies for the %d%c flare at Re =
%0.2f*10^6 m^-1',flare_angle,char(176),Re/10^6);
    title(title_txt)
```

SPOD Visualization

```
mm_pix = 0.081896; %Pixel Scale mm/pixel
P2 = P_cropped;
mi =1; %Mode #s you want to plot
length_f=length(f);
fr_ind(1) =75;
fr_ind(2) =10;
fr_ind(3) =11;
fr_ind(4) =19;
fr_ind(5) =20;
fr_ind(6) =21;
figure;
    tiledlayout(6,1)
fig = figure;
for i = 1:length(fr_ind)
    f(fr_ind(i)); %Output the frequencies to command window
    n = size(P2,2); % n = # of cols
    m = size(P2,1); % m = # of rows

    col_mat = 1:n; % Could also write col_mat = cols to give specific
columns if not starting at column 1
    row_mat = m:-1:1; % row_mat = rows

    fi = fr_ind(i);
    S = squeeze(Pout(fi,:,:,mi));
    S = real(S);
    S = sqrt(abs(S)).*sign(S);
```

```
     nexttile
     hold on

contourf((col_mat)*mm_pix+x_le,row_mat*mm_pix,S,100,'LineStyle','none')
, shading interp, axis equal
     colormap jet
     set(gca,'FontSize',12,'LineWidth',0.5,'FontWeight','demi')
     set(gca,'TickDir','out','Box','on','LineWidth',1)
     set(gca,'YDir','normal')
     txt = sprintf('%d kHz',round(f(fr_ind(i))/1000));
     title(txt)
     ylabel('Y (mm)')
 end
     xlabel('X (mm)')
     title_txt= sprintf('SPOD Mode %d for the %d%c flare at Re =
%0.2f*10^5 m^-1',mi,flare_angle,char(176),Re/10^5);
     sgtitle(title_txt)
```

Bandpass Filtering

```
 % Read and process images
 P3 = zeros(size(P));
 Hd = bandpass_butterworth(fr);

 [numRows, numCols, numFrames] = size(P);
 P_filtered = zeros(size(P));

 % Apply the filter to each pixel
 for row = 1:numRows
     for col = 1:numCols
         pixelTimeSeries = squeeze(P(row, col, :));  % Extract the time
series at each pixel
         % Apply the SOS filter
         filteredPixelTimeSeries = sosfilt(Hd.sosMatrix,
pixelTimeSeries);
         P_filtered(row, col, :) = filteredPixelTimeSeries;  % Store
the filtered time series
     end
 end
```

Bandpass Visualization

```
 % Set the starting frame
 startFrame = 500;
 startTime = 500/fr;
 frameStep = 2;  % Interval of frames
 numImagesToShow = 8;  % Number of images to show

 % Create a figure and use a tiled layout
 figure;
 tiledlayout(numImagesToShow, 1, 'TileSpacing','compact');  % 1 row,
numImagesToShow columns
 % Loop through the desired frames
 for i = 0:numImagesToShow - 1
     % Calculate the frame index
     frameIndex = startFrame + i * frameStep;

     % Check if the frame index exceeds the number of frames
     if frameIndex > size(P_filtered, 3)
         disp(['Frame index ' num2str(frameIndex) ' exceeds the number
of frames.']);
         break;
     end

     % Select the tile and display the image using imagesc
     ax = nexttile;

     imagesc(P_filtered(:,:,frameIndex));
     %title(sprintf('Time = %0.2f ms', (frameIndex/fr)*1e3));
     %colorbar;  % Add a color bar to each subplot to show the scaling
of values

     % Get the size of the current image
     [imgHeight, imgWidth] = size(P_filtered(:,:,frameIndex));

 yticks([])
 xticks([])

     % Adjust color map and scaling
     colormap(ax, gray);  % Set color map to 'jet'
     set(ax, 'Layer', 'top');  % Ensure the axes ticks and labels are
on top of the image
     hold on
```

```
 end
 xticks(ax, linspace(1, imgWidth, 10));  % Set ticks every 10 mm
 %yticks(ax, linspace(1, imgHeight, 4)); % Set ticks across the height
 % Label the ticks in millimeters
 xtick_string = round(x_le:(round(x_le+1024*mm_pix)-
x_le)/9:round(x_le+1024*mm_pix))';
 xtick_string = num2str(xtick_string);
 xticklabels(ax, xtick_string);
     xlabel(ax, 'X (mm)');
     title_txt= sprintf('Butterworth Bandpass Filter (20-40 kHz) for
%d%c flare at Re = %0.2f*10^5 m^-1',flare_angle,char(176),Re/10^5);
     sgtitle(title_txt)
```

Bibliography

[1] Y. Dysa, "Russia Uses Zircon Hypersonic Missile in Ukraine for First Time, Researchers Say," Reuters, Feb 12, 2024.

[2] A. Mehta, “Air Force awards nearly $1 billion contract for a hypersonic cruise missile,” Defense News, 2018.

[3] S. Losey, "Air Force Budget Backs Raytheon Hypersonic, No Lockheed Missile Funds," Defense News, 2024

[4] Araya, G., " Geometry-Independent Hypersonic Boundary Layer Transition Prediction," Johns Hopkins APL Technical Digest, Vol. 36, No. 2, pp. 203-204, 2023

[5] Defense Science Board Task Force, Report of the Defense Science Board Task Force on the National Aerospace Plane (NASP), Defense Science Board, p. 9, Sep. 1988.

[6] T. L. Lewis, R. D. Banner, “Boundary layer transition detection on the X-15 vertical fin using surface-pressure-fluctuation measurements,” Technical report, NASA, 1971.

[7] Lord Rayleigh, “On the question of the stability of the flow of fluids,” The London, Edinburgh, and Dublin philosophical magazine and journal of science, vol. 34, no. 206, pp. 59–70, 1892.

[8] L. Prandtl, “Bemerkungen ´’uber die entstehung der turbulenz,” Journal of Applied Mathematics and Mechanics/Zeitschrift f¨’ur Angewandte Mathematik und Mechanik, vol. 1, no. 6, pp. 431–436, 1921.

[9] L. Prandtl, “Flussigkeitsbewegung, Handworterbuch der Naturwissenschaften,” vol. 4, pp.101-140, 1913.

[10] L. Prandtl, “Uber flussigkeitsbewegung bei sehr kleiner reibung,” ¨ Verhandl. III, Internat. Math.- Kong., Heidelberg, Teubner, Leipzig, pp. 484–491, 1904.

[11] L. Prandtl, “Der luftwiederstad von kugeln,” Nachrichten von der Gesellschaft der Wissenschaften zu G¨ottingen, Mathematisch-Physikalische Klasse, pp. 177–190, 1914. 36

[12] J. D. Anderson, “Ludwig Prandtl’s Boundary Layer,” Physics Today, vol. 58, no. 12, pp. 42-48, Dec. 2005.

[13] D. Bushnell, “Notes on initial disturbance fields for transition problem,” Instability and Transition, pp. 217–232, 1990.

[14] A. Al Hasnine, et al., “Disturbance flow field analysis of particulate interaction with high-speed boundary layers,” AIAA Aviation Forum, p. 3046, 2020.

[15] V. Russo, et al., “Particle-Impingement Simulations for a Hypersonic Flow over a Blunt Cone,” AIAA SciTech Forum, p. 0967, 2021.

[16] L. Paquin, “Effect of Cooling on Hypersonic Boundary layer Stability,” University of Maryland, College Park, MD, 2022.

[17] J. T. Flood, et al. “First and Mack-mode instabilities in a flat-plate boundary layer at Mach 4,” AIAA Scitech Forum, p. 361, 2020.

[18] E. Reshotko, “Boundary layer stability and transition,” Annual review of fluid mechanics, vol. 8, no. 1, pp. 311–349, 1976.

[19] L. M. Mack, “Boundary layer linear stability theory,” Agard rep, vol. 709, no. 3, pp. 1-3, 1984.

[20] C. S. Butler and S. J. Laurence, “Transitional hypersonic flow over slender cone/flare geometries,” J. Fluid Mech., vol. 949, 2022.

[21] C. E. Sousa, et al. “Global analysis of nonlinear second-mode development in a Mach - 6 boundary layer from high-speed schlieren data,” University of Maryland, College Park, MD, 2022.

[22] C. E. Sousa, “Global analysis of transitional hypersonic flow over cone-flare geometries,” Doctoral Dissertation, University of Maryland College Park, 2024.

[23] C. Butler, and S. J. Laurence, "Interaction of Second-Mode Disturbances with an Incipiently Separated Compression-Corner Flow," AIAA Journal, Vol. 59, No. 6, pp. 2034-2046, June 2021.

[24] A. V. Fedorov, A. P. Khokhlov, “Prehistory of instability in a hypersonic boundary layer,” Theoretical and Computational Fluid Dynamics, vol. 14, no. 6, pp. 359–375, 2001.

[25] A. V. Fedorov, “Receptivity of a supersonic boundary layer to solid particulates,” Journal of Fluid Mechanics, vol. 737, pp. 105–131, 2013.

[26] A. Fedorov, “Transition and Stability of High-Speed Boundary Layers,” Annual Review of Fluid Mechanics, vol. 43, pp. 79-95, 2011

[27] A. G. Schoneich, S. J. Laurence, “Development of a Supersonic Ludweig-Tube Facility for Investigating High-Speed Multi-Phase Flows,” University of Maryland, College Park, MD, 2023.

[28] C. Lagares, & G. Araya, “Power spectrum analysis in supersonic/hypersonic turbulent boundary layers,” AIAA SCITECH Forum, 2022.

[29] J. Li, S. Yang, L. Guo, & M. Cheng. “Anisotropic power spectrum of refractive-index fluctuation in hypersonic turbulence,” Applied Optics, 55(32), 9137, 2016.

[30] O. T. Schmidt and T. Colonius, “Guide to spectral proper orthogonal decomposition,” AIAA Journal, vol. 58, no. 3, pp. 1023–1033, 2020.

[31] B. Jones, “Experimental investigation of a boundary layer transition on a slender cone at Mach 4,” Master’s Thesis, University Maryland College Park, 2023.

[32] A. Towne, O. Schmidt, and T. Colonius. Spectral proper orthogonal decomposition and its relationship to dynamic mode decomposition and resolvent analysis. J. Fluid Mechanics, 847: 821–867, 2018.